



Research article

Automated denoising software for calcium imaging signals using deep learning

Sharif Amit Kamran^{a,b}, Hussein Moghnieh^c, Khondker Fariha Hossain^b, Allison Bartlett^a, Alireza Tavakkoli^b, Bernard T. Drumm^d, Kenton M. Sanders^a, Salah A. Baker^{a,*},¹

^a Department of Physiology and Cell Biology, University of Nevada School of Medicine, Reno, NV, 89557, USA

^b Department of Computer Science and Engineering, University of Nevada, Reno, NV 89557, USA

^c Department of Electrical and Computer Engineering, McGill University, Montréal, Québec, H3A 0E9, Canada

^d Department of Life & Health Science, Dundalk Institute of Technology, Co. Louth, Ireland

ARTICLE INFO

Keywords:

Deep learning

Ca²⁺ imaging analysis

Image denoising

Generative adversarial networks

ABSTRACT

Dynamic Ca²⁺ signaling is crucial for cell survival and death, and Ca²⁺ imaging approaches are commonly used to study and measure cellular Ca²⁺ patterns within cells. However, the presence of image noise from instrumentation and experimentation protocols can impede the accurate extraction of Ca²⁺ signals. Removing noise from Ca²⁺ Spatio-Temporal Maps (STMaps) is essential for precisely analyzing Ca²⁺ datasets. Current methods for denoising STMaps can be time-consuming and subjective and rely mainly on image processing protocols. To address this, we developed CalDenoise, an automated software that employs robust image processing and deep learning models to remove noise and enhance Ca²⁺ signals in STMaps effectively. CalDenoise integrates four pipelines capable of efficiently removing salt-and-pepper, impulsive, and periodic noise and detecting and removing background noise. Comprising both an image-processing-based pipeline and three generative-adversarial-network-based (GAN) deep learning models, CalDenoise proficiently removes complex noise patterns. The software features adjustable parameters to enhance accuracy and is integrated into a user-friendly graphical interface for easy access and streamlined usage.

CalDenoise can serve as a robust platform for denoising complex dynamic fluorescence signal images across diverse cell types, including Ca²⁺, voltage, ions, and pH signals.

1. Introduction

Calcium signaling is a vital cellular mechanism that influences a wide range of physiological responses and functions [1,2]. Ca²⁺

Abbreviations: FOV, Field of view; GI, Gastrointestinal; ICC, Interstitial Cells of Cajal; ICC-IM, Intramuscular interstitial cells of Cajal; ICC-MY, Interstitial cells of Cajal at the level of the myenteric plexus; GCaMP, Genetically encoded Ca²⁺ indicator composed of a single GFP; KRB, Krebs Ringer Bicarbonate; ROI, Region of interest; STMap, Spatio-Temporal Map; GAN, Generative Adversarial Network.

* Corresponding author. Department of Physiology and Cell Biology, University of Nevada, Reno School of Medicine, Anderson Medical Building MS352, Reno, NV, 89557, USA.

E-mail address: sabubaker@med.unr.edu (S.A. Baker).

¹ Lead Contact: Further information should be directed to and will be fulfilled by the lead contact, Dr. Sal Baker. Email: sabubaker@med.unr.edu

<https://doi.org/10.1016/j.heliyon.2024.e39574>

Received 27 October 2023; Received in revised form 16 October 2024; Accepted 17 October 2024

Available online 22 October 2024

2405-8440/© 2024 The Author(s). Published by Elsevier Ltd. This is an open access article under the CC BY-NC license (<http://creativecommons.org/licenses/by-nc/4.0/>).

imaging is a broadly utilized technique in medical and biological research, aiding in the study of various cell types, including neurons, smooth muscle cells, and pacemaker interstitial cells, as well as their functions. Cellular Ca^{2+} signals display complex firing patterns with distinct spatial and temporal properties. These signals can manifest as Ca^{2+} waves that propagate within or between cells, lasting from a few seconds to several minutes [3–9], or are stochastic, short-lived signals that occur within milliseconds range [10–13]. Recent developments in Ca^{2+} imaging methods and optogenetic techniques have made it possible to achieve resolution at the subcellular level, providing new insights into the complex nature of Ca^{2+} signaling dynamics within cells. These innovations have led to the generation of vast datasets that demand thorough and efficient analysis. While the hardware for capturing cellular Ca^{2+} signals has evolved significantly, the development of analytical tools to process these signals has lagged behind. Many existing analysis methods struggle to effectively manage the extensive data produced by modern Ca^{2+} imaging technologies.

Most Ca^{2+} imaging systems, such as confocal, light-sheet microscopy, two-photon, or wide-field, are capable of capturing Ca^{2+} signals, but the images often contain varying levels of noise. This noise typically originates from several system hardware sources: 1) Camera-specific noise, such as gain, dark current noise, and photon shot noise, 2) fluctuations in the light source, such as instability in mercury or xenon arc lamps, tungsten-halogen lamps, or LEDs, as well as variations in laser power, and 3) mechanical vibrations within the system.

Signal noise poses a significant challenge in biological imaging research, with tissue fluorescence imaging facing specific issues related to sample noise. Sources of sample noise include autofluorescence, especially when imaging collagen due to its natural autofluorescent properties that overlap with fluorescent dyes; contamination from dyes or sensors and bleed-through between channels can also introduce fluorescence noise. To minimize fluorescence noise and obtain accurate and reliable images it is important to carefully select imaging parameters, optimize sample preparation techniques, and use appropriate controls to account for any potential sources of noise. However, noise present in Ca^{2+} imaging experiments can become superimposed with the collected Ca^{2+} signal datasets, potentially leading to significant inaccuracies during signal extraction and interpretation. As a result, noise reduction is a critical step in analyzing Ca^{2+} imaging data.

One common technique for analyzing and quantifying Ca^{2+} signals is the use of spatio-temporal maps (STMaps). These maps represent intracellular Ca^{2+} signals by plotting them as a function of space and time, providing an effective way to quantify complex Ca^{2+} signaling patterns [5,14–26]. Through Ca^{2+} STMaps analysis, various parameters such as event duration, spatial propagation, frequency, angle, and intensity of Ca^{2+} signals can be measured and analyzed [27–31].

Effectively removing signal noise from the dynamics of the Ca^{2+} sensor is essential for accurately resolving Ca^{2+} signals and processing information from STMaps. Various preprocessing and denoising approaches for Ca^{2+} imaging data have been employed, including image averaging protocols and kernel-based smoothing [32–35]. Ca^{2+} Image averaging is a method that is easy to understand and implement, but it requires a substantial number of images, often difficult to acquire due to photobleaching resulting from prolonged exposure times. Another technique, principal components analysis (PCA), is utilized for reducing noise in image data and extracting cellular signals by simplifying their dimensions [36]. This method identifies and removes dimensions that primarily capture signal noise, but it may also inadvertently discard important information related to Ca^{2+} transient signals and responses to stimuli. A similar PCA-based technique has been employed in neuroimaging to enhance weaker neuronal signals by filtering out background noise in maps of neuronal activity. This method effectively combines traditional difference analysis with principal components analysis. In this approach, the activity map is created by projecting the standard difference onto a basis formed by the principal components that exhibit the highest statistical relevance, while also ensuring that the PCA components exceed a specific correlation threshold with the stimulus distribution [37].

Specific applications also utilize image denoising techniques, such as Fourier analysis, which is effective for morphological imaging of brain activity in response to cyclic stimulation. This method enables signal extraction at the excitation frequency while filtering out activity at other irrelevant frequencies [38–40]. Additionally, another approach uses matrix decomposition to denoise image sequences by taking advantage of the inherent characteristics of the data [41].

The advent of deep learning has led to significant advancements in the accuracy and efficiency of denoising algorithms, largely relying on GPU-powered computation. Significantly, the U-Net architecture and its variants have surpassed traditional machine learning and image processing techniques, establishing themselves as leading solutions for medical image denoising tasks [42–44]. This architecture functions similarly to an auto-encoder and consists of encoder and decoder modules, featuring multiple convolutional layers for both down-sampling and up-sampling. An essential feature of the U-Net architecture is the incorporation of skip connections linking the encoder and decoder, which ensures the retention of high-resolution feature data. The U-Net architecture has found successful application across various imaging techniques, including Computed Tomography (CT), Magnetic Resonance Imaging (MRI) and digital pathology [43]. Additionally, a newer deep learning method known as Generative Adversarial Networks (GANs) employs a generator to create denoised images while using a discriminator to assess whether the generated image matches the true data distribution [45]. Despite the popularity of deep learning models, their potential for denoising Ca^{2+} imaging tasks has not yet been explored. Previous denoising methods typically relied on basic background subtraction, leading to the loss of critical information regarding Ca^{2+} signals and event details. Ca^{2+} STMaps often contain a specific type of periodic noise; typically, periodic noise in images is attributed to system noise and in spinning disk confocal microscopes, this pattern arises from the rotation of the confocal head disks. Factors such as disk speed, laser alignment and imperfections in the microlenses on these disks contribute to the formation of this periodic noise pattern.

Existing denoising techniques lack specific components designed to eliminate periodic and sensor noise. To address this critical issue, we introduce a denoising software that utilizes innovative image-processing techniques alongside three new architectures based on GANs. These techniques successfully filter out noise and enhance Ca^{2+} signals in STMaps, supporting more accurate measurement and analysis of Ca^{2+} activity. Our proposed image-processing method imposes minimal computational demands, making it suitable for

handling large datasets. Furthermore, the GAN architectures leverage GPU acceleration for rapid inference. The overall system includes several hyperparameters that can be adjusted to optimize noise removal from Ca^{2+} signals. Additionally, the parameters of the denoising image-processing modules can be combined in various ways to produce a range of denoised maps of Ca^{2+} signals.

In this study, our denoising software was used to effectively reduce noise and enhance Ca^{2+} signals, resulting in a notable improvement in the signal-to-noise ratio. The objective of this research is to enhance the detection of Ca^{2+} events through machine learning techniques that automatically identify and remove inherent noise in Ca^{2+} maps, optimizing the analysis of these signals. We monitored and obtained Ca^{2+} signals from two different interstitial cell types in the murine colon: submucosal interstitial cells of Cajal (ICC-SM) and intramuscular interstitial cells of Cajal (ICC-IM) [25,46]. Typically, ICC-SM is responsible for generating pacemaker activity in the colon, whereas ICC-IM facilitates neurotransmission [15,47–53]. Each ICC type displays unique Ca^{2+} firing patterns, with ICC-IM exhibiting stochastic firing and ICC-SM demonstrating rhythmic firing [9,52]. Our denoising method was illustrated using ICC Ca^{2+} STMaps, highlighting the accuracy and effectiveness of our model in enhancing Ca^{2+} signals and reduce image noise.

2. Results

2.1. Calcium signal denoising using image processing and generative adversarial networks architectures

Our Calcium Denoising software, CalDenoise, was developed using an image processing module and three state-of-the-art GANs. It includes several innovative components that allow for effective and reliable denoising of subcellular signals which are described below.

2.1.1. Ca^{2+} signal datasets

We utilized datasets from Ca^{2+} STMaps imaged from mice expressing a GCaMP Ca^{2+} sensor in Kit-positive gastrointestinal pacemaker ICCs. These datasets contain subcellular Ca^{2+} signals, which exhibited a range of event patterns, from stochastic to rhythmic, often accompanied by background noise. Within our dataset, signals displayed diverse and complex Ca^{2+} signal patterns. To visualize these dynamic Ca^{2+} signals we generated STMaps which are 2D maps created by reslicing an X-Y-Z section in a movie or image stack. However, these STMaps inherently contain noise and conventional background subtraction and smoothing techniques are

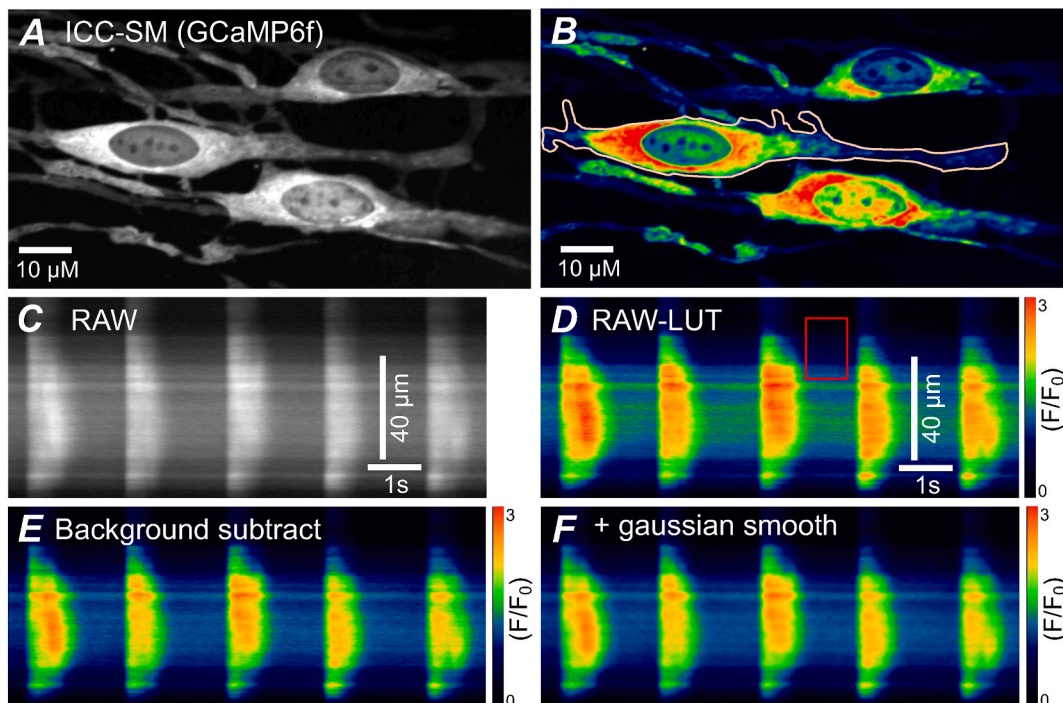


Fig. 1. Background signal noise in Ca^{2+} spatio-temporal maps (STMaps).

A Representative image of ICC-SM from colonic tissues of a Kit-iCre-GCaMP6f mouse. **B** Fluorescence Ca^{2+} intensity image (color-coded), where blue-black represents low fluorescence levels and red-orange represents high Ca^{2+} fluorescence. The pink outline defines the region of interest (ROI) for generating the Ca^{2+} STMap. **C** Representative raw STMap constructed from a single ROI (ICC-SM) indicated in B, plotting the Ca^{2+} signals in 2 dimensions as a function of time. **D** STMap of Ca^{2+} signals in ICC-SM (Color-coded), with the red box highlighting a user-defined ROI for averaging background noise. **E** Representative image of background subtraction noise removal method of Ca^{2+} STMap and additional gaussian filter was applied for signal smoothing. **F** (For interpretation of the references to color in this figure legend, the reader is referred to the Web version of this article.)

not effective in eliminating this noise. To accurately analyze the Ca^{2+} imaging data and other fluorescent dynamic signals present in the STMaps, it is crucial to remove image noise in order to properly define and segment different signal events. Therefore, we developed a novel deep-learning approach based on GANs architecture which achieves highly accurate denoising of Ca^{2+} STMaps. The software consists of four denoising modules as discussed in the following sections.

2.1.2. Denoising of calcium signal maps using image-processing approach

Ca^{2+} signals in colonic ICC-SM were captured using a spinning-disk confocal system (Fig. 1A and B) and pacemaking rhythmic Ca^{2+} transients were recorded and analyzed using STMaps (Fig. 1C and D). STMaps allow the visualization and quantification of both the temporal and spatial characteristics of Ca^{2+} events, along with their intensities, represented through color coding (Fig. 1D). However, while STMap analysis provides an efficient way to quantify Ca^{2+} imaging data, it is prone to several issues, such as artifacts, noise from salt-and-pepper patterns, and impulse noise like light streaks (Fig. 1C–F). These anomalies can interfere with accurate signal extraction.

Traditional techniques, such as background subtraction and Gaussian smoothing filters, are typically applied to reduce noise in

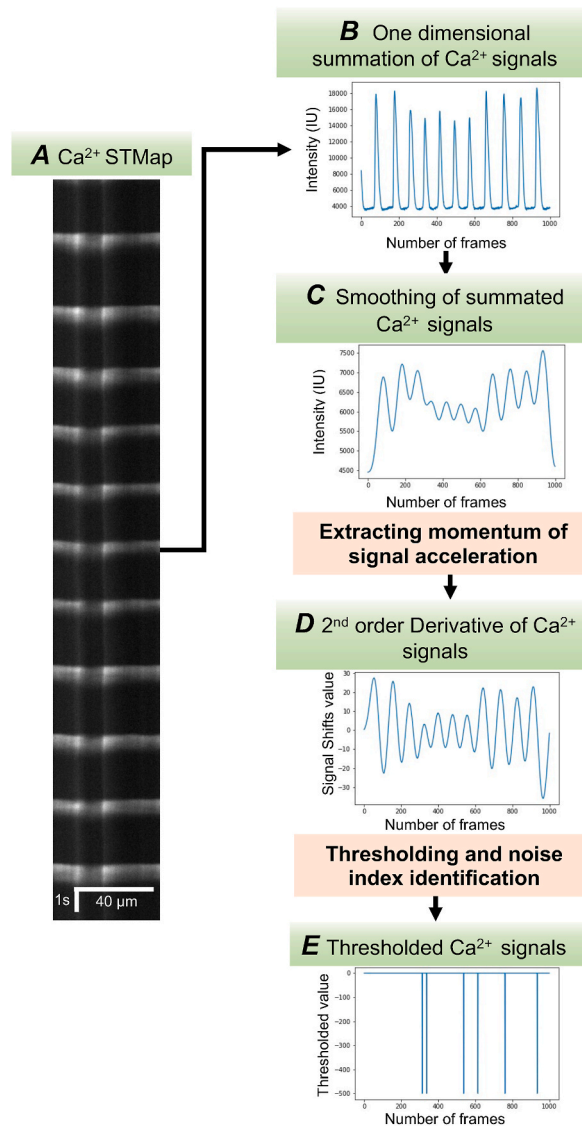


Fig. 2. Momentum extraction and thresholding for noise indices of STMap Ca^{2+} signals.

A Representative image of Ca^{2+} Spatio-temporal map (STMap) of ICC-SM. **B** The Ca^{2+} signals are transformed into one-dimensional data points by summing the intensity signals over the Y-axis of the STMap. **C** Plot of the STMap signal after applying a Gaussian convolution filter, using a kernel size of 3, to smooth the data. **D** A second-order derivative is applied to the one-dimensional signal to detect signal peaks and extract momentum by identifying zero crossings in the STMap. **E** One-dimensional plot of the ICC-SM Ca^{2+} STMap after applying thresholding techniques to locate and define noise indices and signal plateaus.

STMaps. Unfortunately, these methods are not capable of completely eliminating noise without also distorting or reducing the original Ca^{2+} signal (Fig. 1 E and F). To address these challenges, we propose a novel preprocessing and denoising pipeline for STMap analysis. This image-processing denoising approach effectively minimizes artifacts and noise without significantly compromising the integrity of the original Ca^{2+} signals, offering a more refined and accurate method for analyzing Ca^{2+} imaging data.

2.1.3. Calcium signal extraction using Gaussian kernel and Laplacian momentum

We adopted a mathematical approach to define noise, moving away from the conventional image denoising techniques that typically depend on heavy filtering and thresholding. The process begins by aggregating the Ca^{2+} signal values across the X-axis from an individual STMap. This process converts the image data into a one dimensional (1D) cumulative signal (Fig. 2 A&B). This transformation condenses the information, enabling a more computationally efficient analysis of the Ca^{2+} signals. Based on this summated signal, we developed two key equations that describe the behavior of the Ca^{2+} signals as given in Eq. (1) and Eq. (2). Q represents the STMap, where we sum all the values in the i-th row into an intermediate value, T_i as shown in Eq. (2), repeating this summation for each row of Q results in the final 1D signal, T (Fig. 2 B).

$$T_i = \sum_{j=1}^n Q_{ij} \quad (1)$$

$$T = (T_i)_{i=1}^n \quad (2)$$

Our STMaps clearly reveal that the Ca^{2+} signals in ICC-SM exhibit oscillatory behavior, with non-uniform changes in frequency (Fig. 2 B). Once the 2-dimensional Ca^{2+} STMap data was converted into a 1-dimensional data (1D), we applied a Gaussian filter to create a more consistent and smooth signal (Fig. 2 C). The degree of smoothing is controlled by the parameter sigma (σ), which is user-adjustable to accommodate different datasets. To further refine this process, we formulated two key equations Eq. (3) and Eq. (4). In the default configuration, the sigma value is determined by dividing the length of the 1D signal by 40. In Equation (3), the Gaussian filter is denoted as $G(u)$ for 1D signal with the sigma value serving as a variable parameter. Equation (4) presents a 1D convolution operation performed on the input signal $T(x)$ which was derived from Eq. (2), to generate a uniform and smoothed Ca^{2+} signal $V(x)$. It is important to note that convolution, in this case, is a nonlinear process. To ensure proper execution, the signal is padded by 2 prior to applying the convolution, which utilizes a filter size of 3. This padding helps to maintain the integrity of the signal at the boundaries while smoothing it effectively.

$$G(u) = \frac{1}{(\sqrt{2\pi} \cdot \sigma)} \cdot e^{-\left(\frac{u^2}{2\sigma^2}\right)} \quad (3)$$

$$V(x) = T(x) * G(u) \quad (4)$$

To effectively remove noise from STMaps, it is crucial to properly isolate the start and end points of the Ca^{2+} transient signal. This step is essential for eliminating background noise and reducing the overall noise level to zero. We utilized a combination of the Laplacian filter and thresholding techniques to accomplish this. We began by applying the Laplacian filter, specifically a 2nd order derivative, to the filtered 1D Ca^{2+} signal to detect zero-crossings that correspond to changes in the Ca^{2+} signal. These zero-crossings form plateaus that indicate noise indices, which can then be used to filter out noise from the original image (Fig. 2 D). In STMaps,

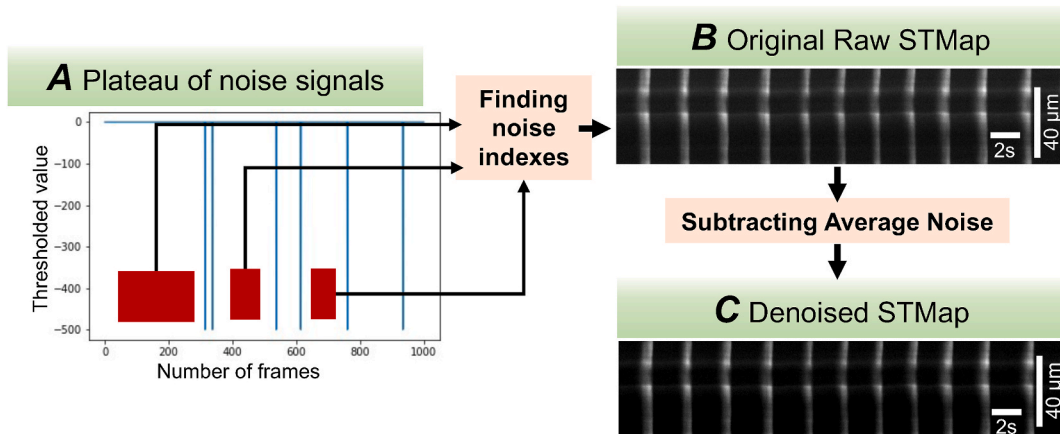


Fig. 3. Mapping and removal of background noise in Ca^{2+} STMaps.

A One-dimensional plot extracted from the ICC-SM Ca^{2+} STMap, with noise indices mapped and marked by red squares. **B** Representative image of raw Ca^{2+} STMap of ICC-SM. **C** Ca^{2+} STMap after subtracting the average noise indices defined in **A**. (For interpretation of the references to color in this figure legend, the reader is referred to the Web version of this article.)

variations in Ca^{2+} signals frequently manifest as vertical line impulses (Fig. 2 B&C). To capture this, we formulated an equation to model the signal using Eq. (5), Where $V(x)$ represents the filtered signal obtained from the previous step in Equation (4) and ∇^2 (nabla) represents the discrete Laplacian operation applied to the 1D signal $V(x)$. The result is $K(x)$, a 1D signal in which the impulses are highlighted as zero-crossings (Fig. 2 E).

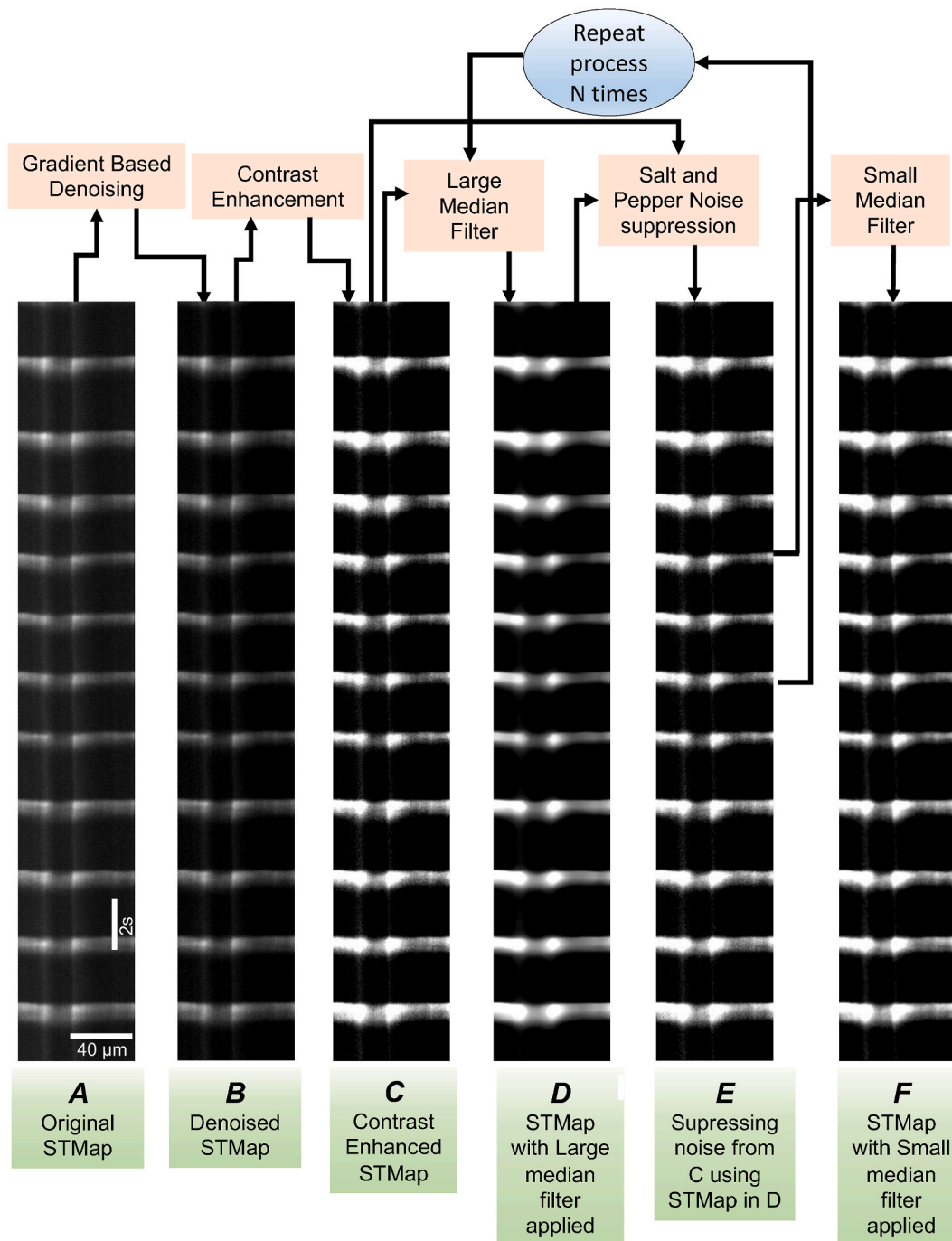


Fig. 4. Calcium signal refinement and noise suppression in STMaps.

A Representative image of denoised Ca^{2+} STMap showing Ca^{2+} events in ICC-SM. **B** Denoised Ca^{2+} STMap after gradient based denoising. **C** Image of Ca^{2+} STMap after applying a contrast enhancement filter to the STMap in A. **D** A large median filter was applied to the Ca^{2+} STMap. **E** Representative image of Ca^{2+} STMap created by subtracting the median-filtered STMap in D from the contrast-enhanced STMap in C, to reduce salt-and-pepper noise. The process can be repeated as needed to achieve the desired level of signal enhancement. **F** Final ICC-SM Ca^{2+} STMap after applying a small median filter. The scale bar in A represents 2 s (y-axis) and 40 μm (x-axis) and applies to all panels B-F.

To accurately identify noise indices and signal spikes, We applied a thresholding algorithm to the Ca^{2+} signal, governed by a conditional Equation (6). In this process, the 1D signal with impulses, denoted as $Z(x)$, is transformed to $Z(x) = -j$, based on the following rule: if $K(x)$ is smaller than predefined t . otherwise, $Z(x)$ is set to zero. $Z(x)$, as noted in (Fig. 2 E). The default value of $j = -500$.

2.1.4. Background noise identification and removal

Once the Ca^{2+} signals and their start and end points have been established, we identify background noise by mapping the plateau indices from the 1D signal to the summated signal. These plateau indices are used to define areas of image noise, allowing for targeted noise subtraction. To achieve this, a window of size 10 is created, ranging from $x + 5$ and -5 , where x represents the plateau index (Fig. 3 A). This window is used to calculate the image noise. If the window extends beyond the boundaries of the 2nd dimension, the window is adjusted to fit within the available range.

After identifying the plateau regions associated with noise, we proceed to calculate the average noise values within these corresponding indices from Eq (1). This total is then divided by the size of the 2nd dimension of the original image to obtain the average noise value for that region.

The calculated average, adjusted by a bias parameter (θ), is subtracted from the raw image to produce the denoised result. Furthermore, the bias parameter (θ) can be customized by the user as a hyperparameter, with a default value of 0.

$$n = (x + 5) - (x - 5), \text{ if } x - 5 < 0 \text{ or } x + 5 > j \quad (7)$$

$$\text{average} = \frac{1}{n} \sum_{i=1}^n W_i \quad (8)$$

$$Y_{ij} = O_{ij} - (\text{average} + \theta) \quad (9)$$

In this method, W represents the noise window, and n is the window size. By default, n is set to 10, unless the lower bound is below zero or the upper bound exceeds the limits of the 2nd dimension of the raw image, as described in Eq. (7). In Eq. (8), The average noise value is then calculated by summing all the values within the noise window, W_j and dividing this sum by the window size (Fig. 4A).

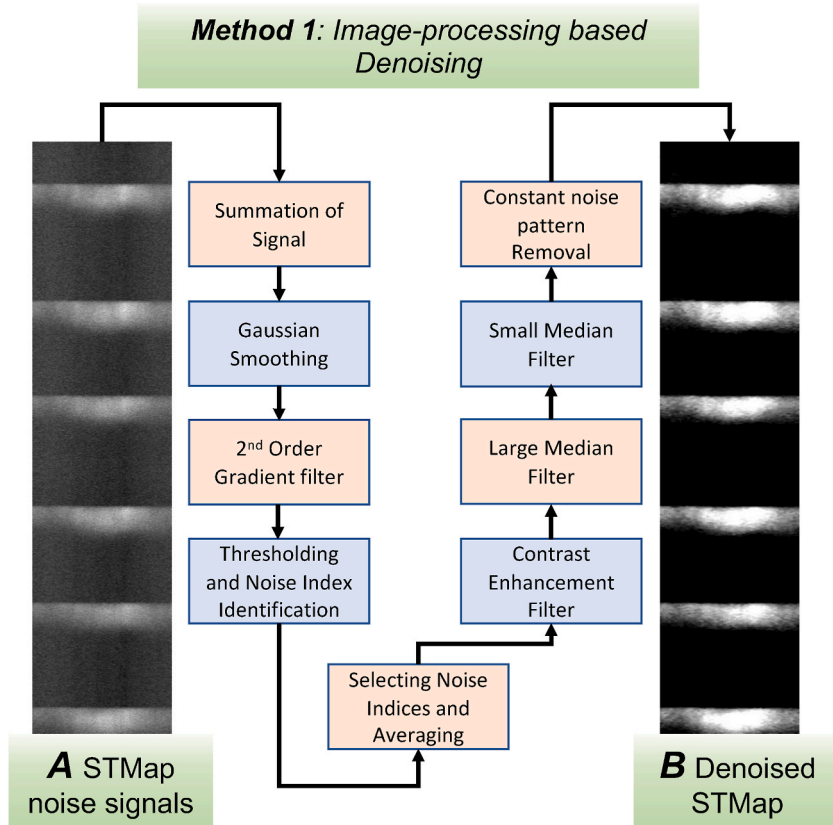


Fig. 5. Image processing method for STMap denoising.

A Representative raw STMap of ICC-SM Ca^{2+} signals. **B** Denoised STMap of Ca^{2+} signals in ICC-SM using the image-processing generated method. **C** Overview of the image-processing-based denoising model developed for STMaps.

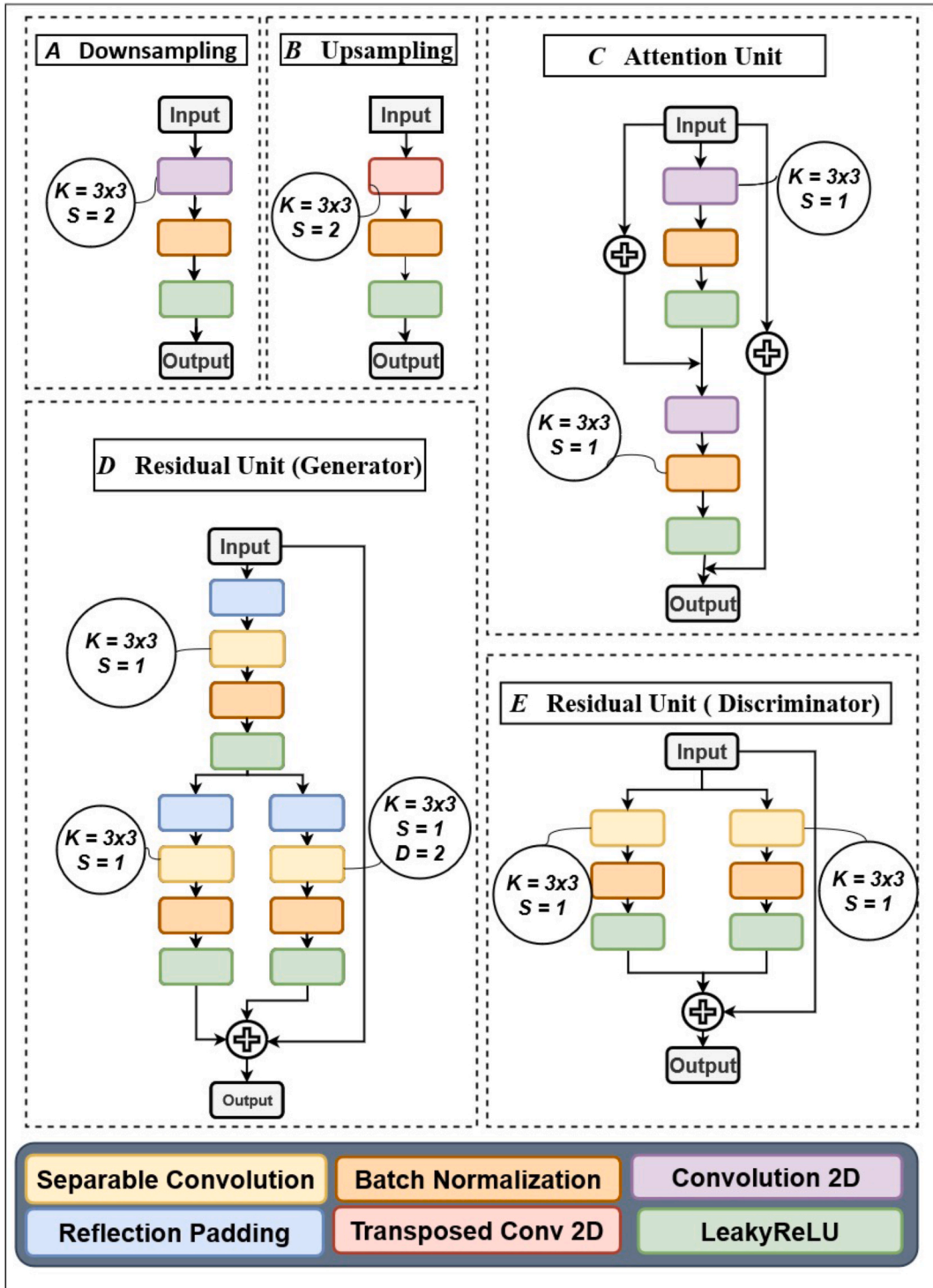


Fig. 6. Key components for generators and discriminators

The denoising generative adversarial network (GAN) architecture comprises several key units: **A** Downsampling unit, **B** Upsampling unit, **C** Attention unit, **D** Residual generator unit, and **E** Residual discriminator unit. Here, K represents kernel size, S denotes stride, and D refers to the dilation rate. The “+” symbol indicates element-wise summation of features along the depth axis.

Next, the calculated average is adjusted by adding a bias θ , which has a default value of 0. This result is then subtracted from the entire original image O_{ij} (Fig. 3B) and Eq (9). The final outcome of this operation is a denoised STMap (Fig. 3C).

2.1.5. Calcium maps noise suppression and contrast enhancement

The final stage of the STMap denoising workflow using the imaging processing module emphasizes the reduction of remaining noise while enhancing the clarity and strength of the Ca^{2+} signals within the STMap. In the case of ICC-SM, a type of pacemaker cell in the colon, this workflow effectively highlights the complex nature of different Ca^{2+} signals and demonstrates the effectiveness of the denoising software and its modules in Ca^{2+} signal analysis (Fig. 4). This denoising process involves several key steps, including the application of a contrast enhancement filter to improve the clarity of the STMap (Fig. 4A and B). Additionally, a large median filter is applied to create a blurred version of the STMap, reducing the impact of outliers and suppressing patterns of salt-and-pepper noise (Fig. 4C and D). From the resulting STMap, pixels with zero values are mapped back into the original image coordinates, which further suppresses noise in the original STMap (Fig. 4E). This process may be repeated as necessary to reach optimal denoising levels. Additionally, a small median filter was applied to denoise the ICC-SM Ca^{2+} STMap (Fig. 4F). This approach has demonstrated equal effectiveness when utilized to ICC-IM STMaps, which display a stochastic and spatially localized firing pattern rather than the oscillatory pattern observed in ICC-SM. The complete denoising workflow, along with all noise suppression and signal enhancement protocols for the STMap Ca^{2+} signals, is described through the following equations.

$$Y_c(i,j) = \text{contrast}[Y(i,j)] \quad (10)$$

$$Y_m(i,j) = \text{median}[Y_c(i,j), i, j \in f] \quad (11)$$

$$O(i,j) = Y_m(i,j), \text{ if } Y_m(i,j) > 0$$

$$\text{or, } O(i,j) = 0, \text{ if } Y_m(i,j) = 0 \quad (12)$$

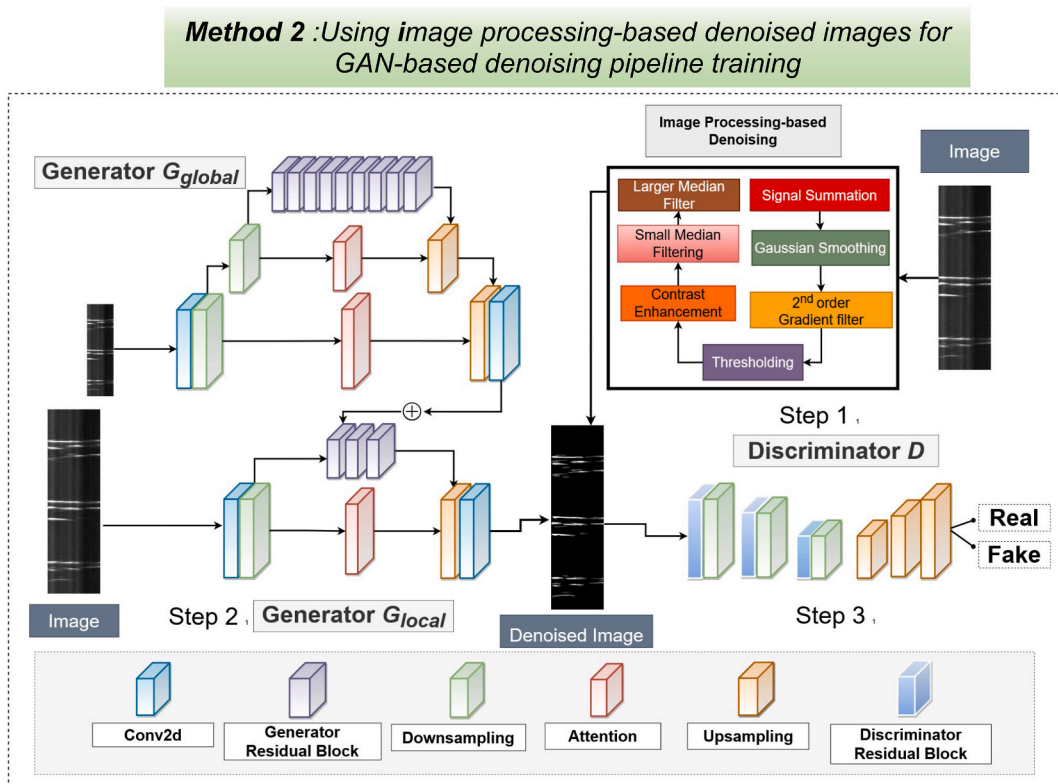


Fig. 7. GAN-based denoising of STMaps with image-processed ground truth.

The denoising generative adversarial network (GAN) pipeline consists of two generators G_{global} , G_{local} , and one discriminator D . **Step 1.** Raw and raw (noisy) Ca^{2+} STMaps are processed through an image-processing-based denoising pipeline to create ground-truth denoised STMaps. **Step 2.** The global generator, G_{global} , processes smaller noisy Ca^{2+} STMaps, producing coarsely denoised outputs. Simultaneously, the local generator takes larger noisy Ca^{2+} STMaps and generates finely denoised STMaps. **Step 3.** The discriminator then takes both the raw noisy Ca^{2+} STMaps and the generated denoised STMaps as input and produces a probability map, indicating whether the input pairs are real or generated (fake). The discriminator employs auto-encoders to produce pixel-wise predictions, determining if each pixel is real or fake.

In this step, we apply a contrast enhancement operation Eq. (10) on the denoised STMap (Figs. 5 and 6), denoted as $Y(i,j)$, which results in a contrast-stretched image $Y_c(i,j)$ (Fig. 4 B). Following this, a median filter f Eq. (11) with a size of 15 is applied, producing the output $Y_m(i,j)$ (Figs. 5 and 6). The output $Y_m(i,j)$ effectively suppresses noise in the raw Ca^{2+} STMap $Y(i,j)$ by eliminating salt and pepper noise outliers (zero pixel values) while preserving the signals in STMaps, as demonstrated in Eq. (12).

The procedure involving the application of the median filter and noise suppression (Eq. (11) and Eq. (12)) is repeated n times, where n is a user-defined hyperparameter, set to 1 by default. In the final step, a median filter size, $f = 3$ is employed to create the denoised STMap (Fig. 4 E). The complete workflow for this image-processing-based denoising of STMaps is summarized and visualized in Fig. 5.

3. Denoising of calcium signals using generative adversarial network (GAN)

Our proposed GAN is detailed in this section and includes descriptions of the building blocks incorporated within the architecture. We also integrated a machine learning approach into the second denoising module of the software to automatically remove noise more efficiently. While the training strategies differ across the three deep learning modules used in the software, their internal architecture and underlying semantics remain consistent.

3.1. GAN-based generator architecture for STMap denoising

To produce fine-grained denoised STMap images as seen in Figs. 7–9, the proposed GAN architecture employs two generators, each constructed with unique building blocks tailored to specific denoising tasks. This dual-generator strategy has proven highly effective for image denoising, as each generator focuses on different aspects of the process, working in tandem to enhance overall image quality.

The integration of two specialized generators, G_{local} and G_{global} , for local and global patch denoising has yielded impressive results in image refinement (Fig. 9). The G_{local} generator focuses on extracting detailed patch-level information, essential for clarifying fine-grained boundaries and reducing periodic noise. On the other hand, the G_{global} generator targets broad-spectrum disturbances such as salt-and-pepper and other visually significant noise types. Both generators employ downsampling and upsampling within their residual

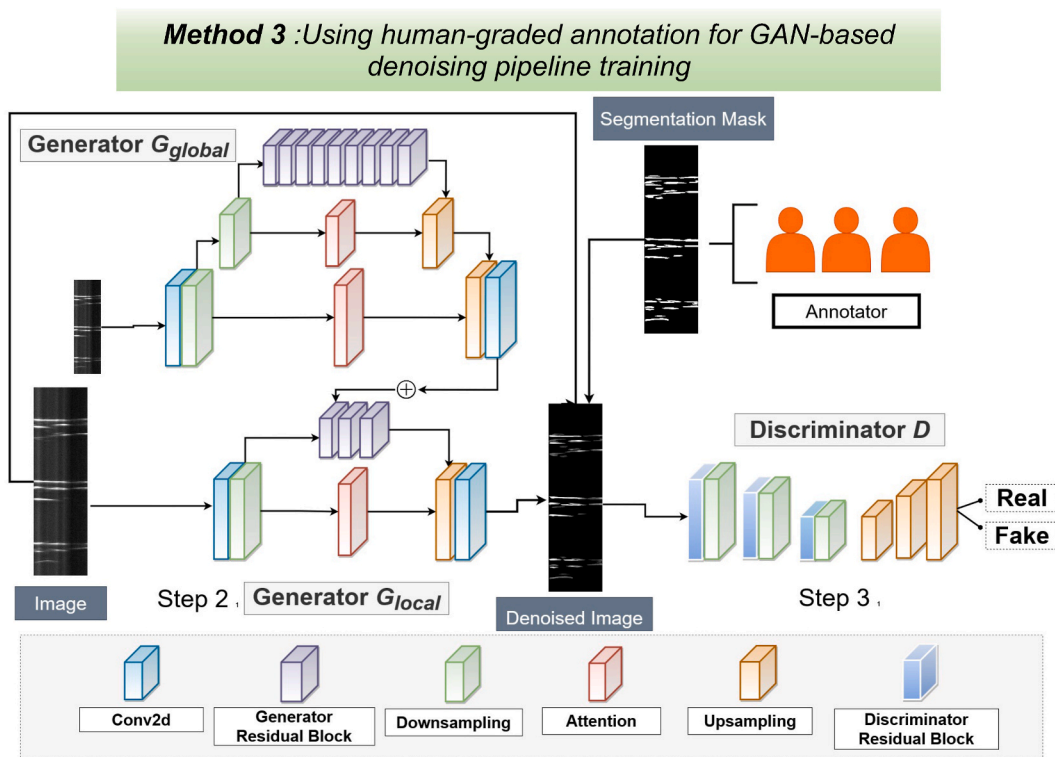


Fig. 8. GAN-based denoising of STMaps with human-annotation ground truth.

The denoising generative adversarial network (GAN) model, consists of two generators G_{global} , G_{local} , and one discriminator D . **Step 1.** The raw Ca^{2+} STMaps are segmented using human annotations to generate ground-truth denoised maps. **Step 2.** The global generator (G_{global}) processes smaller noisy Ca^{2+} STMaps to produce coarsely denoised outputs, while the local generator (G_{local}) handles larger noisy Ca^{2+} STMaps to create finely denoised results.

Step 3. The discriminator then takes both original noisy and denoised Ca^{2+} STMaps as input, generating a probability map that determines whether the pairs are real or fake. The discriminator uses auto-encoders for pixel-wise outputs, deciding the authenticity of each pixel.

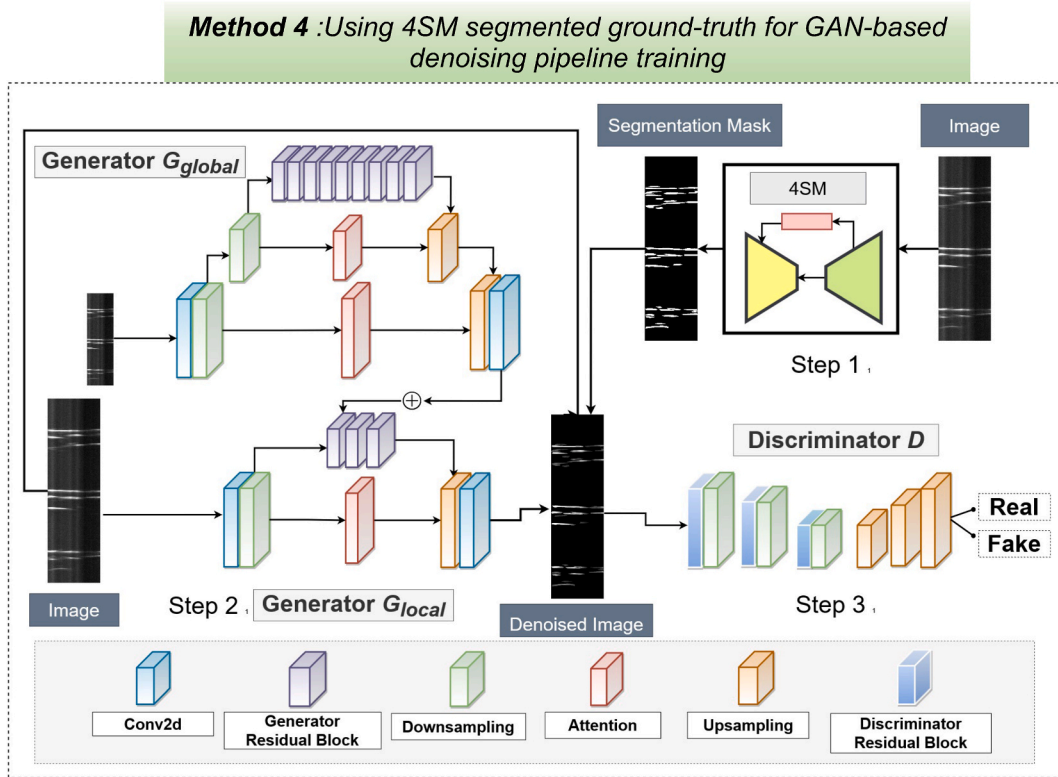


Fig. 9. GAN-based denoising of STMaps with 4SM model ground truth.

The denoising generative adversarial network (GAN), consists of two generators G_{global} , G_{local} , and one discriminator D . **Step 1.** The raw Ca^{2+} STMaps are segmented using the 4SM segmentation model to create ground-truth denoised images. **Step 2.** The global generator (G_{global}) processes smaller noisy Ca^{2+} STMaps, producing coarsely denoised outputs, while the local generator handles larger noisy Ca^{2+} STMaps outputting finely denoised STMaps. **Step 3.** The discriminator takes both original noisy and denoised Ca^{2+} STMaps and denoised Ca^{2+} STMaps as input, producing a probability map that indicates whether the pairs are real or generated (fake). The discriminator utilizes auto-encoders to generate pixel-wise outputs, determining the authenticity of each pixel.

convolution blocks to enhance processing efficiency.

Additionally, an attention block is incorporated to more accurately capture and enhance fine features crucial for denoising sub-cellular boundaries (Fig. 6). G_{local} processes images at a resolution of $64 \times 64 \times 1$, maintaining this resolution in its output, whereas G_{global} works with images at a reduced resolution of $32 \times 32 \times 1$ and similarly outputs images at this resolution. G_{global} also generates a feature vector of size $32 \times 32 \times 64$, which is integrated into G_{local} through a skip connection, enhancing the depth and quality of the denoising process. Further details on each component will be provided in subsequent sections.

3.2. Optimized GAN downsampling and upsampling modules

Traditional non-learnable downsampling and upsampling techniques can result in the loss of crucial spatial features and disrupt the propagation of core information. To address this, we propose two new innovative blocks for both upsampling and downsampling, designed to retain and learn essential feature information for precise denoising through learnable convolution layers (Fig. 6 A&B). These innovative upsampling and downsampling blocks are integral to both the generators and discriminators in our GAN architecture. While the downsampling block is employed in both generators and discriminators, the upsampling block is exclusively used within the generators to produce feature maps and generate the final output.

The downsampling unit block includes a convolutional layer, that integrated and followed by Batch Normalization [54], and activated using a Leaky-ReLU layer (Fig. 6 A). In contrast, the upsampling unit block is constructed with a transposed convolution layer, similarly followed by Batch Normalization [54], and a Leaky ReLU activation layer (Fig. 6 B). This architecture ensures that both upsampling and downsampling can efficiently capture and maintain key spatial features throughout the denoising process.

The downsampling unit is utilized twice after successive residual blocks in both generator models. The upsampling unit block is applied within G_{global} to produce feature outputs that maintain the original spatial dimensions. In G_{local} , it is used once to reconstruct the output at its original spatial resolution. We apply a kernel size of $K=3$ and a stride of $S=2$ to both convolution and transposed convolution layers, maintaining a balanced transformation of the feature maps.

3.3. Optimized residual convolution units

Our architecture incorporates two unique residual blocks: one designed specifically for the generator and the other for the discriminator. A typical residual block consists of two sequential convolution layers and a skip connection that merges the input feature tensor with the resulting output. However, regular convolution layers tend to be less computationally efficient compared to separable convolutions [55]. The key difference is that separable convolution divides the process into depth-wise and point-wise convolution layers, optimizing the retention of both the spatial and depth of signal information. To further enhance feature acquisition, recent studies indicate that merging separable convolution layers with dilation enhances performance [56]. Building on this concept, we designed the generator's residual unit to better preserve depth and spatial information by employing separable convolution, followed by batch normalization and Leaky ReLU activation. This configuration decreases the computational overhead and ensures efficient memory utilization. (Fig. 6 D). Additionally, we incorporate reflection padding before each separable convolution to reuse the values at the borders, padding the input with plausible data.

Through extensive experimentation, we discovered that a wider receptive field captures adjacent, visually significant features more effectively. To achieve this, we enhanced our residual unit by incorporating two branches of separable convolution layers, each utilizing distinct dilation rates: one with a dilation rate of $D=1$ and the other with $D=2$ (Fig. 6 D). Each separable convolution layer employs a kernel size of $K=3$ and a stride of $S=1$, with reflection padding applied before and batch normalization along with Leaky ReLU activation applied afterward. The final output is generated by combining the skip connection from the input with the outputs of both branches.

A comparable method was used to design a customized residual block specifically for the discriminator. This residual block also features two branches of separable convolution layers, followed by batch normalization and Leaky ReLU activation. In the case of the discriminator, both branches use separable convolutions with a kernel size of $K=3$ and stride $S=1$, ensuring effective processing while maintaining computational efficiency.

3.4. Enhanced attention unit components

Repetitive upsampling and downsampling operations often result in the loss of critical spatial information, weakening the model's ability to preserve finer details [57,58]. To overcome this limitation, we introduce an enhanced Attention Unit (Fig. 6C). These attention units act as skip connections, allowing feature information from the lower encoder blocks of the network to be fused with the upper decoder blocks. Each attention unit is composed of two consecutive residual units that include convolution, Batch Normalization, and Leaky ReLU layers. To enhance training speed and stability, Batch Normalization is used to re-centering and re-scaling inputs, while Leaky ReLU helps mitigate the vanishing gradient problem [59]. In this unit, we use a kernel size of $K=3$ and a stride of $S=1$. The first skip connection combines the input with the output of the first residual block, while the second skip connection performs element-wise addition between the input and the output of the final residual block. G_{global} incorporates two attention units, positioned after the downsampling blocks and added successively to the two upsampling blocks. In contrast, G_{local} uses a single attention unit between its downsampling and upsampling blocks.

3.5. Enhanced discriminator architecture for STMap denoising

In our denoising GAN framework, we utilize a single discriminator for G_{local} (Figs. 7–9). Traditionally, GAN discriminators consist of only an encoder, producing small spatial feature outputs to differentiate between real and synthesized images [60–62]. These outputs typically represent patches of the original image, which is why these models are often referred to as Patch-GANs [62]. To improve upon this approach, we introduce a decoder, transforming the discriminator into an auto-encoder designed for pixel-level predictions. This enables the model to determine the authenticity of each individual pixel, rather than just image patches, providing more detailed and fine-grained information to enhance the denoising process for our STMap images. The discriminator processes STMap inputs with a resolution of $64 \times 64 \times 1$, generating feature maps of the same size. Each point in the resulting feature map corresponds to a value within the range of -1 to $+1$, where -1 represents a real pixel and $+1$ indicates a synthesized or adversarial pixel. This pixel-level distinction allows for more precise detection of noise and artifacts, enabling finer control over the denoising process and enhancing the model's ability to differentiate between real and generated data.

3.6. Adversarial objective function

In our GAN architecture, we implemented an adversarial training loss function to estimate the probability of errors and reduce both training and testing inaccuracies. To achieve this, we used a multi-hinge loss for both the discriminator and generator architectures [58,63], as expressed in Eq. (1) and Eq. (2), respectively. To ensure consistency, we normalized all noisy Ca^{2+} STMaps along with their respective ground-truth denoised versions to the range of $[-1, 1]$. In Eq. (3), we combine the outputs of Equations (1) and (2), applying λ_{adv} as a weight multiplier for $L_{\text{adv}}(G)$, as we prioritize the generator's performance over the discriminator to achieve higher quality denoised STMaps.

$$L_{\text{adv}}(D) = - [\min(0, -1 + D(x, x'))] - [\min(0, -1 - D(x, G(x)))] \quad (1)$$

$$L_{\text{adv}}(G) = - [(D(G(x), x'))] \quad (2)$$

$$L_{adv}(G, D) = L_{adv}(D) + \lambda_{adv}(L_{adv}(G)) \quad (3)$$

In the first step (Equation (1)), the discriminator was initially trained on original noisy Ca^{2+} STMaps, denoted as x , and their corresponding real denoised STMaps, denoted as x' , represented by $D(x, x')$. It was then retrained on real noisy Ca^{2+} STMaps, x , paired with synthesized denoised STMaps, $G(x)$ represented as $D(x, G(x))$.

The discriminator, D , underwent several iterations of batch-wise training using randomly sampled data. Once the discriminator was trained, the global generator (G_{global}) was trained while the weights of D remained frozen. Similarly, the local generator (G_{local}) was trained on a batch of randomly sampled noisy STMaps, with the discriminator's weights also frozen during this process. The generators employed the mean squared error loss, as shown in Eq. (2). To ensure that the generated STMaps accurately replicate realistic representations of denoised Ca^{2+} signals. Additionally, we incorporated a discriminator feature loss component, similar to that described in Ref. [62], and formalized in Eq. (5).

$$L_{mse}(G) = \|(G(x) - x')^2\| \quad (4)$$

$$L_{df}(G, D_n) = \sum_{i=1}^p \frac{1}{M} \|D_n^i(x, x') - D_n^i(x, G(x))\| \quad (5)$$

In this context, L_{mse} represents the mean squared loss for a real denoised STMap, x' , given a generated denoised STMap, $G(x)$, where $\|\cdot\|$ denotes the absolute value. The loss function for both G_{global} and G_{local} was employed to ensure that the model produces high-quality denoised STMaps at two different scales. Next, Eq. (6) was estimated first by extracting features from the intermediate layers of the discriminator, first by inputting the real denoised STMaps and then the synthesized denoised STMaps in sequence. M denotes the number of feature layers extracted from the discriminator. $D_n(x, x')$ refers to the intermediate features obtained from the discriminator with a real image as the input, and $D_n(x, G(x))$ pertains to the features extracted when a synthesized image is input.

Finally, the overarching objective for the architecture was established by integrating Eq. (3), Eq. (4), and Eq. (5), as detailed in Eq. (6).

$$\min_{G_f, G_c} ((L_{adv}(G_f, G_c, D, \lambda_{adv})) + \lambda_{mse} [L_{mse}(G_f, G_c)] + \lambda_{df} [L_{df}(G_f, G_c, D)]) \quad (6)$$

In this context, λ_{adv} , λ_{mse} and λ_{df} represent the loss weightings applied to their respective losses. These weightings determine the emphasis placed on different components of the network during training. For our GAN-based models, higher importance is placed on λ_{adv} and λ_{mse} and thus, which is why larger values are chosen for these parameters.

3.7. Image-processing outputs for GAN model training

In our first deep learning GAN-based method, as the ground truth for training, we employed denoised STMaps generated from our improved image-processing protocols described earlier. The overall training architecture and approach are depicted in Fig. 7. In Step 1, the relevant parameters are selected for the image-processing method to denoise the Ca^{2+} STMap. In Step 2, the G_{local} and G_{global} generators take multi-scale of raw and noisy STMaps as input and use the denoised STMaps as ground truth for training. Finally, in Step 3, the discriminator processes pairs of real noisy and denoised STMaps, followed by pairs of real raw and noisy STMaps and generated denoised STMaps, to differentiate between authentic and generated images. It is important to highlight that G_{global} generates only a feature vector, which is then element-wise added to one of the intermediate layers of G_{local} . During the testing phase, only the generators are used to synthesize denoised STMaps, while the discriminators are excluded from the process.

3.8. Human-annotated segmentation for GAN model training

Our second GAN-based training method, utilizes a manually annotated segmentation mask created by a human to generate a denoised Ca^{2+} STMap, which is used as the ground truth as shown in (Fig. 8).

In Step 1, a human annotator is tasked with creating a binary segmentation mask that isolates the Ca^{2+} events in the STMap and separates them from the background. This binary mask is then applied to the noisy STMap, effectively removing all background noise while preserving the foreground. In Step 2, the generators are trained on the noisy STMaps using the manually segmented denoised STMap as the ground truth. Finally, in Step 3, the discriminators are used to differentiate between real and synthesized STMap pairs, ensuring that the model learns to produce high-quality, denoised outputs.

3.9. Deep segmentation model integration for GAN-based denoising

The third GAN-based model utilizes a pre-trained segmentation architecture called the Spatiotemporal Subcellular Signal Segmentation Model (4SM), specifically designed for segmenting Ca^{2+} events in STMaps. 4SM is a GAN architecture optimized for this task, as described in a previous study [64]. In Step 1, the model segments noisy STMaps to create the denoised ground-truth STMaps, as illustrated in (Fig. 9). In Step 2, the G_{local} and G_{global} are trained using pairs of raw (noisy) and denoised STMaps. Finally, in Step 3, the discriminator is employed to differentiate between real and synthesized STMap pairs, ensuring the model's capability to generate high-quality denoised images.

4. Performance assessment of denoising architectures

4.1. Training dataset for denoising GAN models

We optimized our GAN model training using STMaps generated from a diverse set of imaging sequences: 12 Ca^{2+} STMaps derived from ICC-SM and 12 STMaps derived from ICC-IM, captured at various resolutions. To enhance the dataset, we created overlapping 64x64 crops from these images, utilizing a stride of 8 to maximize the use of available data.

For evaluation purposes, the test dataset was assembled from STMaps originating from 6 ICC-SM and 5 ICC-IM videos, providing a robust basis for assessing model performance. The training set contained 37,408 cropped images from ICC-IM and 12,980 cropped images from ICC-SM. The test set included 15,458 cropped images for ICC-IM and 6962 for ICC-SM. Both the noisy and denoised images were collected in grayscale format.

To train the GAN architectures, we employed a leave-one-out cross-validation approach, dividing the dataset into five folds. The training was performed on four folds, with the remaining fold used for validation. Each of the five model versions was tested on the test dataset, and the most accurate version was selected as the primary model. The results for each of our GAN-based techniques are presented in [Tables 1 and 2](#).

4.2. Tuning parameters for GAN training

For hyper-parameter selection, we set $\lambda_{adv} = 10$, $\lambda_{mse} = 10$, and $\lambda_{fm} = 1$ (as described in [Eq. \(6\)](#)). We employed the Adam optimizer [65], with a learning rate of $\alpha = 0.0002$, $\beta_1 = 0.5$ and $\beta_2 = 0.999$. The model was trained using a batch size of $b = 64$ over 150 epochs. Depending on the dataset type: either ICC-IM (stochastic) or ICC-SM (rhythmic) the training process on an NVIDIA V100 GPU took approximately 14–18 h to complete.

4.3. Denoising models evaluation

To assess the effectiveness of our models, we evaluated and compared them to a state-of-the-art deep learning-based auto-encoder model known as U-Net [42]. The U-Net architecture utilizes an encoder-decoder structure with convolutional filters to capture spatial information, progressively downsampling and upsampling to extract multi-depth features. U-Net has been widely adopted across various biomedical imaging applications due to its powerful feature-learning capabilities [66–68].

In [Fig. 10A–F](#), we provide a detailed comparison between predictions from our innovative denoising GAN architectures and U-Net. Our segmentation-based GAN architecture consistently produced superior denoised Ca^{2+} STMaps for ICC-SM, achieving 88 % similarity to the ground truth (GT). In contrast, U-Net struggled to define clear boundaries for Ca^{2+} signals and was unable to effectively remove background noise, positioning our segmentation-based GAN as the more optimal model among the five evaluated.

In the case of Ca^{2+} STMaps generated from ICC-IM, the 4SM-segmentation GAN-based model outperformed all other models, achieving 92.74 % structural similarity, as depicted in [Fig. 10](#). In comparison, U-Net achieved only 59.99 % similarity, highlighting the superior performance of our model in retaining structural details.

To quantitatively evaluate the denoising performance of Ca^{2+} STMaps, we employed two key metrics: 1) Structural Similarity Index Measure (SSIM), a standard metric used to assess image quality degradation by measuring perceptual similarity. 2) Peak Signal-to-Noise Ratio (PSNR), which evaluates the quality of the reconstructed images.

We present the 5-fold cross-validated results for our models, evaluated in terms of SSIM and PSNR, in [Tables 1–3](#). For ICC-SM, the segmentation-based GAN was our top performer, achieving 88.75 % structural similarity and a PSNR of 24.64 ([Table 1](#)). For ICC-IM, the 4SM-based GAN demonstrated superior performance, with a structural similarity of 92.74 % and a PSNR of 25.88 ([Table 2](#)). Additionally, we compared the 4SM-segmentation model against U-Net, and the results in [Table 3](#) show that the 4SM model significantly outperformed U-Net in both SSIM and PSNR metrics. Finally, we analyzed the strengths and weaknesses of each denoising approach, comparing them in terms of speed and accuracy, as outlined in [Table 4](#).

5. Graphical user interface for CalDenoise denoising pipelines

To simplify the use of the denoising modules for STMaps and enhance user experience, we developed a graphical user interface (GUI) for CalDenoise, our Python-based tool designed for efficient denoising of subcellular Ca^{2+} fluorescent signals. The GUI was built using PyQt, an open-source Python library. One of the key advantages of PyQt is that it allowed us to create a user-friendly interface without the need for additional frameworks. Moreover, the software is platform-independent and can run on any operating system that

Table 1
Quantitative Results for ICC-SM (Rhythmic) test images for denoising.

Denoising Models	SSIM	PSNR
Image-Process Denoising	25.49 %	21.49
GAN-denoising	61.72 %	22.95
Segmentation GAN-denoising	88.75 %	24.64
4SM GAN-denoising	84.97 %	23.20

Table 2
Comparative Results for ICC-IM (Stochastic) test images for denoising.

Denoising Models	SSIM	PSNR
Image-Process Denoising	27.45 %	21.67
GAN-denoising	59.64 %	24.92
Segmentation GAN-denoising	91.98 %	26.96
4SM GAN-denoising	92.74 %	25.88

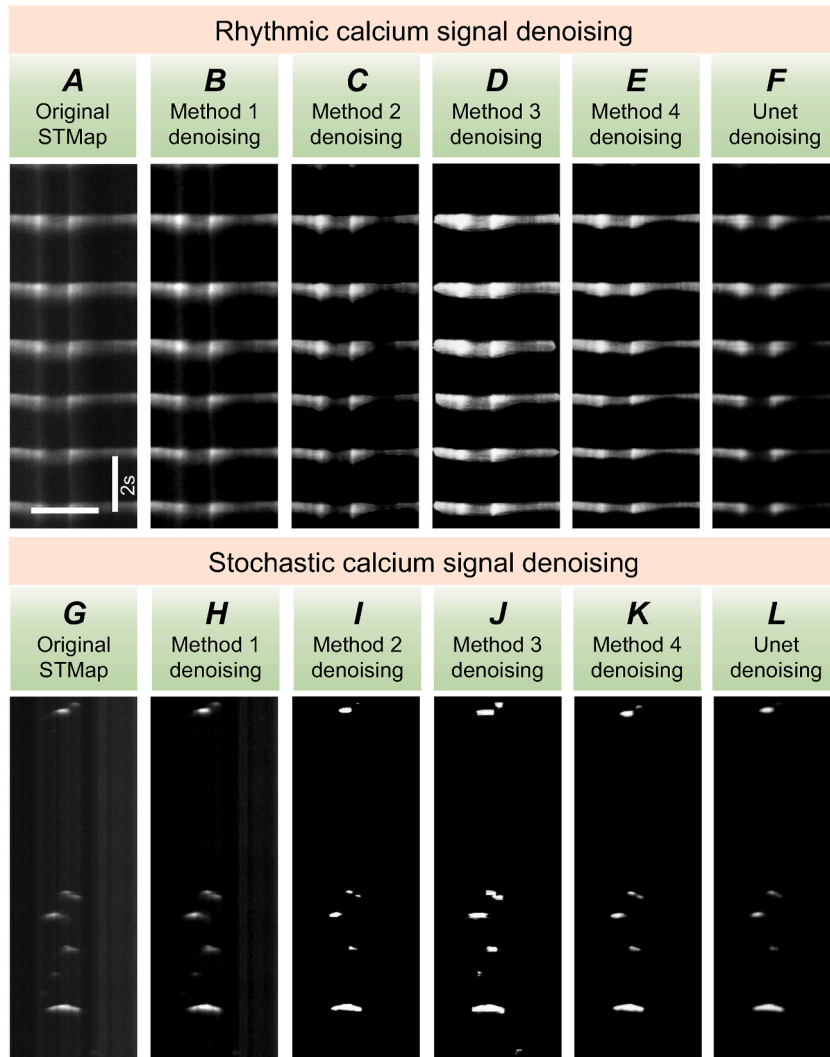


Fig. 10. Comparing denoising methods for stochastic and rhythmic Ca^{2+} signals.

A Representative image of raw STMap of Ca^{2+} signals in ICC-SM. **B** Denoised output from the image-processing-based method. **C** Denoised output from the image-processing-based GAN trained method. **D** Denoised output from the segmentation-based GAN trained method. **E** Denoised output from the 4SM-based GAN trained method. **F** Denoised output from U-Net method. The scale bars in A represent $x = 2 \text{ s}$ and $y = 10 \mu\text{m}$. **G** Representative raw STMap of Ca^{2+} signals in ICC-IM. **H-L** Corresponding denoised outputs from the same image-processing pipelines: image-processing (method 1, **H**), image-processing-based GAN (method 2, **I**), segmentation-based GAN (method 3, **J**), 4SM-based GAN (method 4, **K**), and U-Net denoising (**L**), respectively. The scale bars in A also apply to G.

supports Python.

The CalDenoise interface offers four distinct denoising methods, all of which are accessible via an intuitive GUI (Fig. 11). Users can batch process datasets for faster denoising and can easily upload input images using drag-and-drop functionality. The interface provides a real-time display of the denoising results, allowing users to adjust the degree of denoising by selecting from the four methods available (Fig. 11A). Additionally, all denoising parameters are fully customizable, giving users granular control over the process

Table 3
Comparative Results between U-Net and our best GAN-based denoising pipeline.

Denoising Models	SSIM	PSNR
U-Net (ICC-SM)	61.31 %	21.67
U-Net (ICC-IM)	59.99 %	23.92
4SM GAN-denoising (ICC-SM)	84.97 %	23.20
4SM GAN-denoising (ICC-IM)	92.74 %	25.88

Table 4
Advantages and disadvantages of each of the denoising approaches.

Technique	Inference Speed (second)	Training with Annotated Masks	Manual Parameter Tuning	Hardware	SSIM (ICC-SM)	SSIM (ICC-IM)
Image-processing Based	0.09	No	Required	CPU	25.49 %	27.45 %
GAN-denoising	0.1	No	Not required	GPU	61.72 %	59.64 %
Segmentation GAN-denoising	0.1	Yes	Not required	GPU	88.75 %	91.98 %
4SM GAN-denoising	0.1	No	Not required	GPU	84.97 %	92.74 %

(Fig. 11B and C).

Once the denoising is complete, the denoised maps can be compared, saved, and exported for further analysis and interpretation, all within the tool itself (Fig. 11D).

6. Discussion

Ca²⁺ signaling is a major aspect of cell survival and death. Technological advancements in Ca²⁺ indicators, biosensors and imaging instruments provide exceptional spatial and temporal resolution for imaging cellular Ca²⁺ signals. However, extracting Ca²⁺ dynamics data is laborious and time-consuming due to the complexity and variability of Ca²⁺ signal patterns across cell types. STMaps are a common method to analyze Ca²⁺ transients but their effectiveness is hindered by suboptimal instrumentation and experimental noise. Challenges currently exist to effectively remove imaging noise and analyze STMaps in a fast, accurate, and standardized method. Previous denoising protocols for Ca²⁺ images and STMaps mostly relied on subjective background subtraction methods to define noise pixel ROIs and many of these protocols ignored the dynamic and nonuniform nature of image noise all together. The present study focuses on STMap noise removal in an effective, uniform, dynamic, fast, and unbiased method to enhance Ca²⁺ signals and achieve more accurate Ca²⁺ signal detection and quantification. Here, we've proposed four automated image-processing and deep learning based denoising modules for a STMap analysis pipeline to help researchers carry out essential denoising of Ca²⁺ STMaps swiftly and with little overhead for computation. The proposed model is very fast with the average inference time for image-processing to final output is 80–90 ms (ms). In contrast, the deep learning model's output is around 100–120 ms (ms) per single image crop. This efficient computation time includes all the denoising filter and noise model mapping and computation associated with each step. The method also can be used for batch processing of images, a feature within the software that enables the simultaneous processing of multiple image files rather than handling single images one at a time. This approach improves efficiency by allowing batch image processing and is particularly useful when working with large datasets. Our image-processing pipeline can also generate filtered images to enable user evaluation and adjustment of the denoising degree at each given step. Summation of Ca²⁺ signals over time is a method commonly used for finding peaks of active signals in Ca²⁺ imaging [34,35,69,70]. In our approach, we utilize the signal peak function to allow identification of noise indices and the denoising module which incorporates a zero-crossings function, commonly used for edge detection methods [71–73], to define the noise indices and active signal indices for proper denoising of Ca²⁺ STMaps. This process allows effective and accurate separation of noise indices from the active signal and ensures that only noise was discriminated rather than active signals.

Fluorescent signal photobleaching is a common issue in Ca²⁺ imaging that causes the average signal intensity to decrease over time, affecting both noise and active signal indices. Therefore, the background noise index must be defined from the noise indices. In the image processing denoising module the average noise index was selected from the noise plateau signal's highest pixel values which was shown to effectively remove salt and pepper or random telegraph noise while minimizing background noise. In addition, the image-processing denoising module includes a contrast enhancement filter to improve the active Ca²⁺ signal. Multiple consecutive median filters were employed to ensure removal of salt and pepper or random telegraph noise from STMaps. To preserve active signals that may be disrupted by applying the filters to the resulting images, we used inverse mapping in the pipeline before applying each filter.

In typical image background subtraction methods, a region of interest (ROI) with the appearance of a noisy background is manually selected by the user. The task involves averaging the pixel intensity of that area and subtracting or dividing the selected pixel values from the entire image. While this method can remove salt and pepper noise to some degree, it is ineffective against impulsive noise and constant background noise that may have higher pixel intensity than the actual signal. Furthermore, these methods are subjective and lack consistency as user judgment may vary. Other background noise removal methods have been employed in imaging preprocessing, such as Fourier analysis [38–40], PCA [36,37] and Matrix decomposition [41]. Although these techniques can reduce image noise,

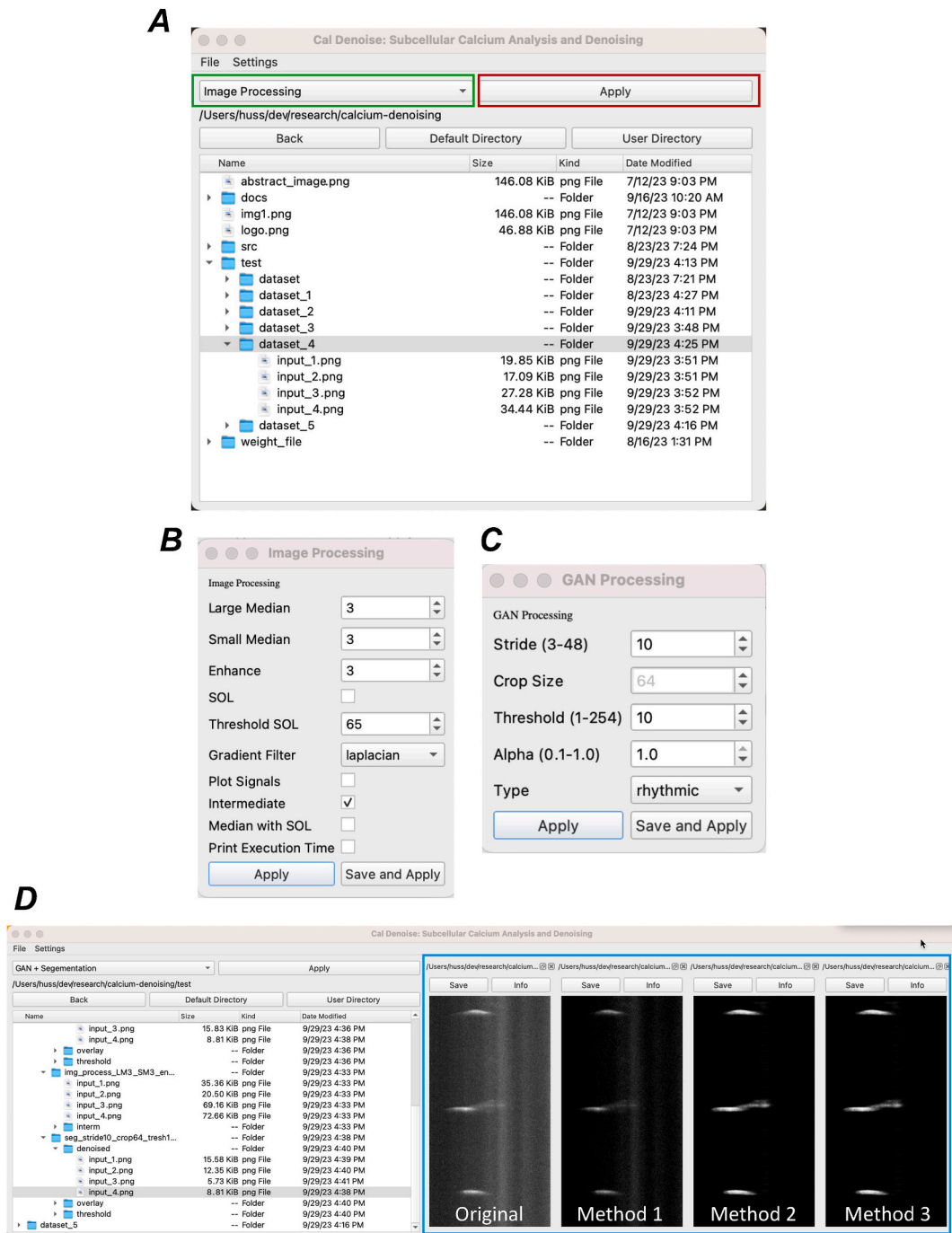


Fig. 11. Features of CalDenoise interface

A Representative view of the CalDenoise interface, showing user-controlled denoising model selection (green box) and model settings (red box). **B&C** Each denoising model provides a parameter selection window, allowing users to input their preferred settings. **D** The interface displays the original and denoised STMaps (blue box), helping users compare results from different denoising models and adjust settings accordingly. A comparison of STMap denoising outputs from various CalDenoise models is also shown in D. (For interpretation of the references to color in this figure legend, the reader is referred to the Web version of this article.)

they can also cause image signal degradation, miss certain signal frequencies, and allow for the persistent presence of noise and artifacts.

Distinguishing between signal and noise within cells is complex. Non-dynamic signals, along with low-intensity or diffuse fluorescence, can make it challenging to identify true dynamic signals. Additionally, noise from external sources or artifacts can further

obscure cellular signals and affect the clarity of dynamic signal detection. Our approach primarily focused on enhancing intracellular dynamic signals, though we recognize that basal fluorescence and non-dynamic signals may also be affected by the software. While our method effectively isolates dynamic signals, it may still influence basal fluorescence to some extent.

The U-Net architecture has become a prevalent standard for medical image denoising tasks due to recent advancements in deep learning [42–44]. It has shown success in various applications including digital pathology, dermatoscopy, MRI, and CT images [43]. However, the proposed 3 novel GAN architecture-based denoising pipelines surpassed U-Net's denoising capabilities by providing more accurate denoising and enhanced Ca^{2+} signals in STMaps with higher qualitative and quantitative metrics. Additionally, our model's parameter count is only 3.34 million, which is 10-times less than that of U-Net. In our proposed machine learning approach we established three different ground truths. The first approach used an image-processing-based technique as the ground truth for training and the other two approaches employed segmentation mask-based noise removal with human annotation and a GAN-based model, respectively. To evaluate the results, we used structural similarity index (SSIM) and peak signal-to-noise ratio (PSNR) to assess structural similarity and signal quality between the original and denoised signals. Additionally, ground truths enhanced dynamic signal extraction by primarily focusing on dynamic and non-dynamic signals which reduced basal background fluorescence and improved overall signal analysis.

7. Conclusions

Our novel denoising techniques leverage various deep learning and image processing approaches to deliver an automated, swift, and precise STMap denoising protocol for a wide range of Ca^{2+} imaging. This effectively eliminates a variety of noise types that STMaps are prone to including background, impulsive, sensor, periodic, and low-frequency noise. Given that these types of signal noise can hinder the Ca^{2+} data extraction from STMaps, it is crucial to integrate such a module in the Ca^{2+} imaging analysis and data retrieval pipelines.

8. Limitations of the study

This study introduces a novel solution for efficiently and accurately removing image noise from dynamic cellular Ca^{2+} and fluorescent signals. However, for optimal performance and speed, our software relies on more recent GPU technology, which can be expensive and may restrict accessibility. It's important to note that this limitation is not unique to CalDenoise, as most deep learning architectures rely on GPU-based computations. Consequently, the software's utilization in commonly used image analysis tools like Image J is limited. Despite these constraints, the CalDenoise software offers rapid and precise noise removal for cellular fluorescent signals facilitating seamless signal analysis. To improve the robustness and accuracy of image processing algorithms, software enhancement and development are required to incorporate a wider range of image noise modalities. This is essential for effectively handling the diverse noise patterns that may exist in various image datasets.

9. STAR★Methods

9.1. Key resources table

REAGENT or RESOURCE	SOURCE	IDENTIFIER
Experimental models: Organisms/strains		
GCaMP6f-floxed mice (B6; 129S-Gt(ROSA)26Sor ^{tm95.1(CAG-GCaMP6f)Hze/J})	Jackson Laboratories	Strain #:024105 RRID:IMSR_JAX:024105
Kit-Cre mice (c-Kit ^{+/Cre-ERT2})	Provided by Dr. Dieter Saur	https://doi.org/10.1113/JP271699
Software and algorithms		
Fiji, version 2.0.0-rc-69/1.52	NIH	https://fiji.sc/
4SM, Subcellular Fluorescence Analysis Software	GitHub	https://doi.org/10.1016/j.isci.2022.104277 ; https://github.com/SharifAmit/CalciumGAN/tree/main
STMapAuto, Ca^{2+} Analysis plugin	GitHub	https://doi.org/10.1016/j.ceca.2020.102260

10. Method details

10.1. Experimental model and subject details

10.1.1. Animals

GCaMP6f mice (B6.129S-Gt(ROSA)26Sor^{tm38(CAG-GCaMP3)Hze/J}) and their control counterparts (C57BL/6) were obtained from Jackson Laboratories (Bar Harbor, MN, USA). These were crossed with Kit-iCre mice (c-Kit^{+/Cre-ERT2}), from Dr. Dieter Saur (Technical University Munich, Munich, Germany). Tamoxifen was administered at 6–8 weeks of age, as previously described [13].

10.1.2. Tissue preparation

Segments of the colon, each 2 cm long, were excised from Kit-iCre-GCaMP6f mice and placed in Krebs-Ringer bicarbonate solution (KRB) following established protocols [13]. Each segment was longitudinally opened along the mesenteric border, and contents were gently rinsed off. Selective dissection was used to separate either the mucosal or the muscular layers. The prepared tissue samples, either submucosa or muscle, were then stretched out and secured onto Sylgard-lined dishes.

10.1.3. Calcium imaging

Colonic sheets were perfused with 37 °C KRB solution and were equilibrated for a period of 1 h, as previously described [13,28]. A spinning-disk confocal microscope (CSU-W1 spinning disk; Yokogawa Electric Corporation) was used for all Ca²⁺ imaging experiments. The confocal head is connected to a Nikon Eclipse FN1 microscope equipped with a 40x 0.8 NA CFI Fluor lens (Nikon instruments INC, NY, USA). Laser at 488 nm wavelength was directed using a Borealis system (ANDOR Technology, Belfast, UK). EMCCD Camera (Andor iXon Ultra; ANDOR Technology, Belfast, UK) was used to capture the GCaMP6f emission. Images were acquired at 33 frames per second using MetaMorph software (Molecular Devices INC, CA, USA).

10.1.4. Calcium event analysis

Analysis of Ca²⁺ activity in ICC was performed as previously described [13,28]. Briefly, movies of Ca²⁺ activity in ICC (30 s long) were converted to a stack of tagged image file format (TIFF) images and imported into custom software (Volumetry G8.a) for analysis. The whole-cell ROIs were used to generate STMaps of Ca²⁺ activity in individual ICC.

10.1.5. Download and installation of software

For successful software operation, the system should have 1) a GPU-enabled system with CUDA version 10.0+ installed and 2) Anaconda, a Python package and environment management tool, installed. The code can be downloaded from the following GitHub repository: <https://github.com/SharifAmit/CalDenoise>. Once downloaded, please follow the instructions in the README.md file for installing and running the denoising program.

Data and code availability

The original software “CalDenoise” is an open-source and publicly available from.

GitHub: <https://github.com/SharifAmit/CalDenoise>.

Further information necessary for reanalyze the data reported in this paper can be obtained from the lead contact upon request.

CRedit authorship contribution statement

Sharif Amit Kamran: Writing – review & editing, Writing – original draft, Validation, Software, Investigation, Formal analysis, Data curation, Conceptualization. **Hussein Moghnieh:** Writing – review & editing, Writing – original draft, Visualization, Validation, Supervision, Software, Methodology, Formal analysis, Data curation. **Khondker Fariha Hossain:** Validation, Formal analysis. **Allison Bartlett:** Writing – original draft, Visualization, Data curation. **Alireza Tavakkoli:** Writing – review & editing, Validation, Supervision, Resources, Conceptualization. **Bernard T. Drumm:** Writing – review & editing, Writing – original draft, Visualization, Validation. **Kenton M. Sanders:** Writing – review & editing, Funding acquisition, Conceptualization. **Salah A. Baker:** Writing – review & editing, Writing – original draft, Visualization, Supervision, Software, Resources, Project administration, Methodology, Investigation, Funding acquisition, Data curation, Conceptualization.

11. Materials availability

The software code developed in this study has been uploaded to GitHub: <https://github.com/SharifAmit/CalDenoise>.

All relevant data are provided within the main text.

Ethics statement

All procedures followed the NIH Guide for the Care and Use of Laboratory Animals and were approved by the University of Nevada, Reno’s IACUC (Protocol ID: 21-02-1131-1).

Funding

This project was supported by R01 DK-120759 from the National Institute of Diabetes and digestive and Kidney (NIDDK).

Declaration of competing interest

The authors declare that they have no known competing financial interests or personal relationships that could have appeared to influence the work reported in this paper.

Acknowledgements

The authors would like to thank the Computational Modeling and Analysis core supported by the NIH (P30-GM145646) and Nevada Bridge to AI-enabled Scientific & Engineering Computing (NvBAISEC) supported by the NSF (OAC-2201599) for their computer services.

Data and materials availability

All data are available in the main text and the codes are available from repository: <https://github.com/SharifAmit/CalDenoise>.

References

- [1] M.J. Berridge, P. Lipp, M.D. Bootman, The versatility and universality of calcium signalling, *Nat. Rev. Mol. Cell Biol.* 1 (2000) 11–21.
- [2] K.M. Sanders, B.T. Drumm, C.A. Cobine, S.A. Baker, Ca, *Physiol. Rev.* 104 (2024) 329–398.
- [3] S.V. Straub, D.R. Giovannucci, D.I. Yule, Calcium wave propagation in pancreatic acinar cells: functional interaction of inositol 1, 4, 5-trisphosphate receptors, ryanodine receptors, and mitochondria, *J. Gen. Physiol.* 116 (2000) 547–560.
- [4] G.W. Hennig, N.J. Spencer, S. Jokela-willis, P.O. Bayguinov, H.t. Lee, L.A. Ritchie, S.M. Ward, T.K. Smith, K.M. Sanders, ICC-MY coordinate smooth muscle electrical and mechanical activity in the murine small intestine, *Neuro Gastroenterol. Motil.* 22 (2010) e138–e151.
- [5] H. Cheng, M.R. Lederer, W. Lederer, M. Cannell, Calcium sparks and $[Ca^{2+}]_i$ waves in cardiac myocytes, *Am. J. Physiol. Cell Physiol.* 270 (1996) C148–C159.
- [6] F.X. Boittin, N. Macrez, G. Halet, J. Mironneau, Norepinephrine-induced Ca^{2+} waves depend on $InsP(3)$ and ryanodine receptor activation in vascular myocytes, *Am. J. Physiol.* 277 (1999) C139–C151.
- [7] S.A. Baker, G.W. Hennig, A.K. Salter, M. Kurahashi, S.M. Ward, K.M. Sanders, Distribution and Ca^{2+} signalling of fibroblast-like (PDGFR α +) cells in the murine gastric fundus, *J. Physiol.* 591 (2013) 6193–6208.
- [8] M.J. Berridge, P. Lipp, M. Bootman, Calcium signalling, *Curr. Biol.* 9 (1999) R157–R159.
- [9] B.T. Drumm, C.A. Cobine, S.A. Baker, Insights on gastrointestinal motility through the use of optogenetic sensors and actuators, *J. Physiol.* 600 (2022) 3031–3052.
- [10] M.D. Bootman, M.J. Berridge, The elemental principles of calcium signaling, *Cell* 83 (1995) 675–678.
- [11] J.H. Jaggard, V.A. Porter, W.J. Lederer, M.T. Nelson, Calcium sparks in smooth muscle, *Am J Physiol Cell Physiol* 278 (2000) C235–C256.
- [12] I. Parker, J. Choi, Y. Yao, Elementary events of $InsP_3$ -induced Ca^{2+} liberation in *Xenopus* oocytes: hot spots, puffs and blips, *Cell Calcium* 20 (1996) 105–121.
- [13] S.A. Baker, B.T. Drumm, D. Saur, G.W. Hennig, S.M. Ward, K.M. Sanders, Spontaneous Ca^{2+} transients in interstitial cells of Cajal located within the deep muscular plexus of the murine small intestine, *J. Physiol.* 594 (2016) 3317–3338.
- [14] C.J. Roome, B. Kuhn, Simultaneous dendritic voltage and calcium imaging and somatic recording from Purkinje neurons in awake mice, *Nat. Commun.* 9 (2018) 3388.
- [15] H.T. Lee, G.W. Hennig, K.J. Park, P.O. Bayguinov, S.M. Ward, K.M. Sanders, T.K. Smith, Heterogeneities in ICC Ca^{2+} activity within canine large intestine, *Gastroenterology* 136 (2009) 2226–2236.
- [16] B.T. Drumm, G.W. Hennig, S.A. Baker, K.M. Sanders, Applications of spatio-temporal mapping and particle analysis techniques to quantify intracellular Ca^{2+} signaling in situ, *J. Vis. Exp.* (2019).
- [17] M.A. Colman, C. Pinali, A.W. Trafford, H. Zhang, A. Kitmitto, A computational model of spatio-temporal cardiac intracellular calcium handling with realistic structure and spatial flux distribution from sarcoplasmic reticulum and t-tubule reconstructions, *PLoS Comput. Biol.* 13 (2017) e1005714.
- [18] R. Waadt, M. Krebs, J. Kudla, K. Schumacher, Multiparameter imaging of calcium and abscisic acid and high-resolution quantitative calcium measurements using R-GECO1-mTurquoise in *Arabidopsis*, *New Phytol.* 216 (2017) 303–320.
- [19] K.J. Park, G.W. Hennig, H.T. Lee, N.J. Spencer, S.M. Ward, T.K. Smith, K.M. Sanders, Spatial and temporal mapping of pacemaker activity in interstitial cells of Cajal in mouse ileum in situ, *Am J Physiol Cell Physiol* 290 (2006) C1411–C1427.
- [20] S.L. Dargan, B. Schwaller, I. Parker, Spatiotemporal patterning of IP_3 -mediated Ca^{2+} signals in *Xenopus* oocytes by Ca^{2+} -binding proteins, *J. Physiol.* 556 (2004) 447–461.
- [21] C.A. Cobine, K.I. Hannigan, M. McMahon, E.P. Ni Bhraonain, S.A. Baker, K.D. Keef, Rhythmic calcium transients in smooth muscle cells of the mouse internal anal sphincter, *Neuro Gastroenterol. Motil.* 32 (2020) e13746.
- [22] T.B. Bolton, D.V. Gordienko, Confocal imaging of calcium release events in single smooth muscle cells, *Acta Physiol. Scand.* 164 (1998) 567–575.
- [23] S.A. Baker, B.T. Drumm, K.E. Skowronek, B.E. Rembetski, L.E. Peri, G.W. Hennig, B.A. Perrino, K.M. Sanders, Excitatory neuronal responses of Ca^{2+} transients in interstitial cells of cajal in the small intestine, *eNeuro* 5 (2018).
- [24] W.A. Leigh, G. Del Valle, S.A. Kamran, B.T. Drumm, A. Tavakkoli, K.M. Sanders, S.A. Baker, A high throughput machine-learning driven analysis of Ca, *Cell Calcium* 91 (2020) 102260.
- [25] S.A. Baker, S.J. Hwang, P.J. Blair, C. Sirekci, L. Wei, S. Ro, S.M. Ward, K.M. Sanders, Ca^{2+} transients in ICC-MY define the basis for the dominance of the corpus in gastric pacemaking, *Cell Calcium* 99 (2021) 102472.
- [26] S.A. Baker, B.T. Drumm, K.E. Skowronek, B.E. Rembetski, L.E. Peri, G.W. Hennig, B.A. Perrino, K.M. Sanders, Excitatory neuronal responses of Ca^{2+} transients in interstitial cells of cajal in the small intestine, *eNeuro* (2018).
- [27] B.T. Drumm, G.P. Sergeant, M.A. Hollywood, K.D. Thornbury, N.G. McHale, B.J. Harvey, The role of cAMP dependent protein kinase in modulating spontaneous intracellular Ca^{2+} waves in interstitial cells of Cajal from the rabbit urethra, *Cell Calcium* 56 (2014) 181–187.
- [28] S.A. Baker, B.T. Drumm, C.A. Cobine, K.D. Keef, K.M. Sanders, Inhibitory neural regulation of the Ca^{2+} transients in intramuscular interstitial cells of cajal in the small intestine, *Front. Physiol.* 9 (2018) 328.
- [29] G.P. Sergeant, L. Johnston, N.G. McHale, K.D. Thornbury, M.A. Hollywood, Activation of the cGMP/PKG pathway inhibits electrical activity in rabbit urethral interstitial cells of Cajal by reducing the spatial spread of Ca^{2+} waves, *J. Physiol.* 574 (2006) 167–181.
- [30] M. Sancho, E. Bradley, A. Garcia-Pascual, D. Triguero, K.D. Thornbury, M.A. Hollywood, G.P. Sergeant, Involvement of cyclic nucleotide-gated channels in spontaneous activity generated in isolated interstitial cells of Cajal from the rabbit urethra, *Eur. J. Pharmacol.* 814 (2017) 216–225.
- [31] S. Fedigan, E. Bradley, T. Webb, R.J. Large, M.A. Hollywood, K.D. Thornbury, N.G. McHale, G.P. Sergeant, Effects of new-generation TMEM16A inhibitors on calcium-activated chloride currents in rabbit urethral interstitial cells of Cajal, *Pflugers Arch* 469 (2017) 1443–1455.
- [32] J. Schummers, H. Yu, M. Sur, Tuned responses of astrocytes and their influence on hemodynamic signals in the visual cortex, *Science* 320 (2008) 1638–1643.
- [33] L.M. Martinez, J.M. Alonso, R.C. Reid, J.A. Hirsch, Laminar processing of stimulus orientation in cat visual cortex, *J. Physiol.* 540 (2002) 321–333.
- [34] J.N. Kerr, D. Greenberg, F. Helmchen, Imaging input and output of neocortical networks in vivo, *Proc Natl Acad Sci U S A* 102 (2005) 14063–14068.
- [35] A. Basole, L.E. White, D. Fitzpatrick, Mapping multiple features in the population response of visual cortex, *Nature* 423 (2003) 986–990.
- [36] E.A. Mukamel, A. Nimmerjahn, M.J. Schnitzer, Automated analysis of cellular signals from large-scale calcium imaging data, *Neuron* 63 (2009) 747–760.
- [37] M. Gabbay, C. Brennan, E. Kaplan, L. Sirovich, A principal components-based method for the detection of neuronal activity maps: application to optical imaging, *Neuroimage* 11 (2000) 313–325.
- [38] T. Mrcic-Flogel, M. Hübener, T. Bonhoeffer, Brain mapping: new wave optical imaging, *Curr. Biol.* 13 (2003) R778–R780.
- [39] V.A. Kalatsky, M.P. Stryker, New paradigm for optical imaging: temporally encoded maps of intrinsic signal, *Neuron* 38 (2003) 529–545.
- [40] A. Sornborger, C. Sailstad, E. Kaplan, L. Sirovich, Spatiotemporal analysis of optical imaging data, *Neuroimage* 18 (2003) 610–621.

- [41] Q. Li, L. Qi, G. Bi, W. Li, Denoising for bio-image sequences via matrix decomposition. 2014 IEEE China Summit & International Conference on Signal and Information Processing (ChinaSIP), IEEE, 2014, pp. 515–519.
- [42] O. Ronneberger, P. Fischer, T. Brox, U-net: convolutional networks for biomedical image segmentation. *International Conference on Medical Image Computing and Computer-Assisted Intervention*, Springer, 2015, pp. 234–241.
- [43] S. Nasrin, M.Z. Alom, R. Burada, T.M. Taha, V.K. Asari, Medical image denoising with recurrent residual u-net (r2u-net) base auto-encoder. 2019 IEEE National Aerospace and Electronics Conference (NAECON), IEEE, 2019, pp. 345–350.
- [44] M.P. Heinrich, M. Stille, T.M. Buzug, Residual U-net convolutional neural network architecture for low-dose CT denoising, *Current Directions in Biomedical Engineering* 4 (2018) 297–300.
- [45] I. Goodfellow, J. Pouget-Abadie, M. Mirza, B. Xu, D. Warde-Farley, S. Ozair, A. Courville, Y. Bengio, Generative adversarial networks, *Commun. ACM* 63 (2020) 139–144.
- [46] S.A. Baker, W.A. Leigh, G. Del Valle, I.F. De Yturriaga, S.M. Ward, C.A. Cobine, B.T. Drumm, K.M. Sanders, Ca(2+) signaling driving pacemaker activity in submucosal interstitial cells of Cajal in the murine colon, *Elife* 10 (2021) e64099.
- [47] S. Yoneda, H. Fukui, M. Takaki, Pacemaker activity from submucosal interstitial cells of Cajal drives high-frequency and low-amplitude circular muscle contractions in the mouse proximal colon, *Neuro Gastroenterol. Motil.* 16 (2004) 621–627.
- [48] B. Lies, V. Gil, D. Groneberg, B. Seidler, D. Saur, E. Wischmeyer, M. Jimenez, A. Friebe, Interstitial cells of Cajal mediate nitergic inhibitory neurotransmission in the murine gastrointestinal tract, *Am. J. Physiol. Gastrointest. Liver Physiol.* 307 (2014) G98–G106.
- [49] B.T. Drumm, S.J. Hwang, S.A. Baker, S.M. Ward, K.M. Sanders, Ca(2+) signalling behaviours of intramuscular interstitial cells of Cajal in the murine colon, *J. Physiol.* 597 (2019) 3587–3617.
- [50] K.M. Sanders, Y. Kito, S.J. Hwang, S.M. Ward, Regulation of gastrointestinal smooth muscle function by interstitial cells, *Physiology* 31 (2016) 316–326.
- [51] B.T. Drumm, B.E. Rembetski, K. Huynh, A. Nizar, S.A. Baker, K.M. Sanders, Excitatory cholinergic responses in mouse colon intramuscular interstitial cells of Cajal are due to enhanced Ca, *FASEB J* (2020).
- [52] K.M. Sanders, B.T. Drumm, C.A. Cobine, S.A. Baker, Ca, *Physiol. Rev.* (2023).
- [53] K.M. Sanders, L.F. Santana, S.A. Baker, Interstitial cells of Cajal - pacemakers of the gastrointestinal tract, *J. Physiol.* (2023).
- [54] S. Ioffe, C. Szegedy, Batch normalization: accelerating deep network training by reducing internal covariate shift. *International Conference on Machine Learning*, PMLR, 2015, pp. 448–456.
- [55] F. Chollet, Xception: deep learning with depthwise separable convolutions. *Proceedings of the IEEE Conference on Computer Vision and Pattern Recognition*, 2017, pp. 1251–1258.
- [56] S.A. Kamran, A. Tavakkoli, S.L. Zuckerbrod, Improving robustness using joint attention network for detecting retinal degeneration from optical coherence tomography images, in: 2020 IEEE International Conference on Image Processing (ICIP), IEEE, 2020, pp. 2476–2480.
- [57] X. Chen, C. Xu, X. Yang, D. Tao, Attention-gan for object transfiguration in wild images. *Proceedings of the European Conference on Computer Vision, ECCV*, 2018, pp. 164–180.
- [58] H. Zhang, I. Goodfellow, D. Metaxas, A. Odena, Self-attention generative adversarial networks. *International Conference on Machine Learning*, PMLR, 2019, pp. 7354–7363.
- [59] A.L. Maas, A.Y. Hannun, A.Y. Ng, Rectifier nonlinearities improve neural network acoustic models, *Proc. icml*, Citeseer (2013) 3.
- [60] K.-B. Park, S.H. Choi, J.Y. Lee, M. gan, Retinal blood vessel segmentation by balancing losses through stacked deep fully convolutional networks, *IEEE Access* 8 (2020) 146308–146322.
- [61] Y. Choi, Y. Uh, J. Yoo, J.-W. Ha, Stargan v2: diverse image synthesis for multiple domains. *Proceedings of the IEEE/CVF Conference on Computer Vision and Pattern Recognition*, 2020, pp. 8188–8197.
- [62] T.-C. Wang, M.-Y. Liu, J.-Y. Zhu, A. Tao, J. Kautz, B. Catanzaro, High-resolution image synthesis and semantic manipulation with conditional gans. *Proceedings of the IEEE Conference on Computer Vision and Pattern Recognition*, 2018, pp. 8798–8807.
- [63] J.H. Lim, J.C. Ye, Geometric gan. *arXiv Preprint arXiv:1705.02894*, 2017.
- [64] S.A. Kamran, K.F. Hossain, H. Moghnieh, S. Riar, A. Bartlett, A. Tavakkoli, K.M. Sanders, S.A. Baker, New open-source software for subcellular segmentation and analysis of spatiotemporal fluorescence signals using deep learning, *iScience* 25 (2022) 104277.
- [65] D.P. Kingma, J. Ba, Adam: a method for stochastic optimization. *arXiv Preprint arXiv:1412.6980*, 2014.
- [66] M.Z. Alom, M. Hasan, C. Yakopcic, T.M. Taha, V.K. Asari, Recurrent Residual Convolutional Neural Network Based on U-Net (R2u-net) for Medical Image Segmentation, 2018 *arXiv preprint arXiv:1802.06955*.
- [67] M.Z. Alom, C. Yakopcic, M. Hasan, T.M. Taha, V.K. Asari, Recurrent residual U-Net for medical image segmentation, *Journal of Medical Imaging* 6 (2019) 014006.
- [68] J. Zhuang, LadderNet: Multi-Path Networks Based on U-Net for Medical Image Segmentation, 2018 *arXiv preprint arXiv:1810.07810*.
- [69] W.Q. Malik, J. Schummers, M. Sur, E.N. Brown, Denoising two-photon calcium imaging data, *PLoS One* 6 (2011) e20490.
- [70] A. Giovannucci, J. Friedrich, M. Kaufman, A. Churchland, D. Chklovskii, L. Paninski, E.A. Pnevmatikakis, Onacid: online analysis of calcium imaging data in real time, *Adv. Neural Inf. Process. Syst.* (2017) 2381–2391.
- [71] O. Lalgant, F. Truchetet, A nonlinear derivative scheme applied to edge detection, *IEEE Trans. Pattern Anal. Mach. Intell.* 32 (2008) 242–257.
- [72] R.M. Haralick, Digital step edges from zero crossing of second directional derivatives, *IEEE Trans. Pattern Anal. Mach. Intell.* 6 (1984) 58–68.
- [73] L. Ding, A. Goshtasby, On the Canny edge detector, *Pattern Recogn.* 34 (2001) 721–725.